Materials Today Advances 6 (2020) 100071

Contents lists available at ScienceDirect

Materials Today Advances

journal homepage: www.journals.elsevier.com/materials-today-advances/

CO_2 transformation to multicarbon products by photocatalysis and electrocatalysis

C. Du [a, b, c], X. Wang [a, b, d], W. Chen [c], S. Feng [d], J. Wen [a, b], Y.A. Wu [a, b, *]

[a] Department of Mechanical and Mechatronics Engineering, University of Waterloo, Waterloo, Ontario, N2L 3G1, Canada
[b] Waterloo Institute for Nanotechnology, University of Waterloo, Waterloo, Ontario, N2L 3G1, Canada
[c] State Key Laboratory of Electroanalytical Chemistry, Changchun Institute of Applied Chemistry, Chinese Academy of Science, Changchun, Jilin, 130022, PR China
[d] State Key Laboratory of Inorganic Synthesis and Preparative Chemistry, College of Chemistry, Jilin University, Changchun, Jilin, 130012, PR China

ARTICLE INFO

Article history:
Received 2 March 2020
Received in revised form
20 March 2020
Accepted 26 March 2020
Available online 26 April 2020

Keywords:
CO_2 reduction reaction
C_{2+} products
Photocatalytic
Electrocatalytic
Selectivity

ABSTRACT

The excessively high atmospheric CO_2 concentration is associated with rapidly evolving industrial, commercial, and residential uses of fossil fuels, which has caused global warming and climate crisis. Photocatalytic or electrocatalytic reduction of CO_2 into value-added hydrocarbon fuels has provided a promising and sustainable solution to addressing these issues simultaneously. Multicarbon products (C_{2+}) with higher energy densities are generally desirable in fueling transportation and other industries. However, the low selectivity and subsequently a higher cost toward these C_{2+} products have severely limited their larger scale production. Here, we review the strategies of controlling the C_{2+} product selectivity during the photocatalytic and electrocatalytic CO_2 reduction reaction (CRR) processes with their catalytic reaction mechanisms. This review starts with the fundamentals on photocatalytic and electrocatalytic CRR, which is followed by discussions about how reaction mechanisms and process pathways affect the C_{2+} product selectivity and the main strategies to improve both photocatalysis and electrocatalysis systems. Finally, some outlook for future work and challenges in improving the C_{2+} product selectivity is included.

1. Introduction

Fossil fuel has been the primary power source for human activities since the first industrial revolution, with an 11-fold increase in its consumption rate [1–3]. Overexploitation and excessive utilization of fossil fuels has not only led to a crisis of energy use but also caused extremely serious greenhouse gas (such as CO_2) emissions which result in climate change. Typically, the concentration of atmospheric CO_2 has dramatically increased from approximately 280 ppm in the early 1800s to currently 385 ppm, and it may reach nearly 600 ppm in 2100 [4]. A rapid increase of CO_2 concentration in the atmosphere would raise the global mean temperature and result in island shrinking, desert expansion, and possibly species extinction. Therefore, reducing the atmospheric CO_2 concentration as well as increasing its utilization is of vital importance.

Capturing and converting CO_2 into value-added hydrocarbon fuels has provided a solution to addressing carbon emission and energy crises simultaneously. Especially, the solar energy–driven CO_2 conversion into hydrocarbon fuels has showed a great commercialization potential, benefitting from renewable energy use and zero release of pollutants [5]. Specifically, photocatalytic and electrocatalytic CO_2 reduction reaction (CRR) processes are two major approaches which can convert CO_2 into useful products by directly or indirectly utilizing solar energy. Their major difference is the source of electrons involved in the catalysis process. Namely, the electrons in photocatalysis are mainly derived from the excitons of semiconductor photocatalysts by the photonic excitation, while the electrons in electrocatalysis are principally originated from an external electric field. Notably, the external electrical energy can be supplied from the photovoltaic solar cells, and thus, electrocatalysis can indirectly utilize solar energy to convert CO_2. In both photocatalytic and electrocatalytic systems, CO_2 molecules usually tend to be reduced into C_1 products, such as CO, formic acid, methanol, etc. [6] However, from the perspective of economic value, the production of higher order multicarbon products (C_{2+}) is more

* Corresponding author.
E-mail address: yimin.wu@uwaterloo.ca (Y.A. Wu).

https://doi.org/10.1016/j.mtadv.2020.100071

desirable than that of C_1 products, owing to their higher energy densities and a wider applicability [7]. Consequently, the design of catalysts to increase the efficiency and selectivity toward C_{2+} products remains as a big challenge in this field. Until now, extensive theoretical and experimental studies have suggested that the successful production of C_{2+} products is closely related to various elemental reaction steps, reaction conditions, and the catalyst selection [8]. Therefore, studying the CRR mechanism, reaction conditions, as well as catalyst structures is of great significance to improve the C_{2+} product selectivity in the CRR process.

In this review, we focus on the progress of controlling C_{2+} product selectivity during the photocatalytic and electrocatalytic CRR processes. First, the fundamentals of photocatalytic and electrocatalytic CRR are introduced. Then, the main strategies toward improving C_{2+} product selectivity are comprehensively discussed. Be noted that the selectivity discussed in this review is exclusively based on the C_{2+} product selectivity, namely the competition between C_1 product and multicarbon C_{2+} products rather than the competition between CRR and hydrogen evolution reaction (HER). The overview on the CRR selectivity under the competition with HER can be found in some recent reviews [9–12]. Finally, some outlook for future work and challenges in improving C_{2+} product selectivity are also presented.

2. Fundamentals of the CO_2 reduction reaction

2.1. Mechanism of photocatalytic CO_2 reduction

Photocatalytic CO_2 reduction is one of the technologies for 'artificial photosynthesis,' which aims at mimicking the natural photosynthesis process. It converts atmospheric CO_2 to chemical fuels, coupled with the H_2O/O_2 cycle, and uses sunlight as the sole energy input [13,14]. In nature, the photosynthesis process plays an essential role in sustaining the ecosystem by providing essential energy for most lives and propelling the carbon/oxygen cycle on the earth. Natural photosynthesis is usually achieved by green plants and consists of two sequential steps, i.e., the light reaction and the dark reaction [15]. As seen in Fig. 1A, during the light reaction, chlorophyll first adsorbs sunlight and then transforms it into chemical energy which can be stored in the adenosine triphosphate (ATP), and meanwhile, H_2O is oxidized into O_2. In the dark reaction, driven by the energy stored in ATP, CO_2 is finally stepwise reduced into carbohydrates. Similar to the natural photosynthesis processes, photocatalytic CO_2 reduction can be divided into three principal steps: (i) light absorption, (ii) charge separation, and (iii) surface reactions, as schemed in Fig. 1B [16]. Light absorption (step i) refers to the process that the photocatalyst (usual semiconductor) absorbs photons from sunlight and generates excitons which are electron and hole pairs. Under the illumination of sunlight, electrons in the semiconductor will be excited from the valence band (VB) to the conduction band (CB), leaving an equal number of holes in VB. Those photogenerated electrons in the CB will be used for CO_2 reduction, while the photogenerated holes in the VB will be used for water oxidation in the following steps. However, to make those electrons and holes energetically favorable for the following reaction, semiconducting photocatalysts should be designed with an appropriate band structure. Typically, the CB edge should be higher (more negative) than the redox potential of CO_2 reduction indicated in Eqs. (1)–(7), while the VB edge needs to be lower (more positive) than the redox potential of water oxidation at about 1.23 V against normal hydrogen electrode (NHE) (pH = 0) (Fig. 2). To overcome the large overpotentials of the two electrochemical reactions, the bandgap should be sufficiently large. Nevertheless, a too large bandgap would limit the utilization of the most of the solar spectrum. For example, TiO_2 with a large bandgap of 3.2 eV can only absorb radiation in the ultraviolet domain ($\lambda < 400$ nm), which accounts for less than 5% of the total solar spectrum [17]. As a

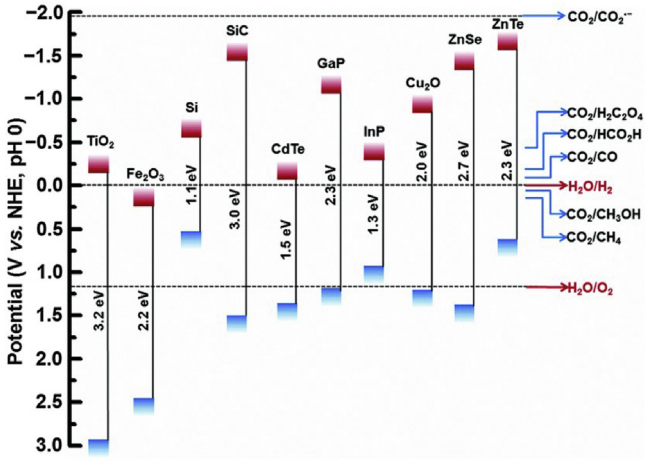

Fig. 2. CB (red squares) and VB (blue squares) positions of some common semiconductor photocatalysts and the redox potentials vs. NHE of CRR and water splitting under pH 0 condition. CB, conduction band; VB, valence band; NHE, normal hydrogen electrode; CRR, CO_2 reduction reaction. Reproduced with permission from Chang et al. [18]. Copyright 2016, The Royal Society of Chemistry.

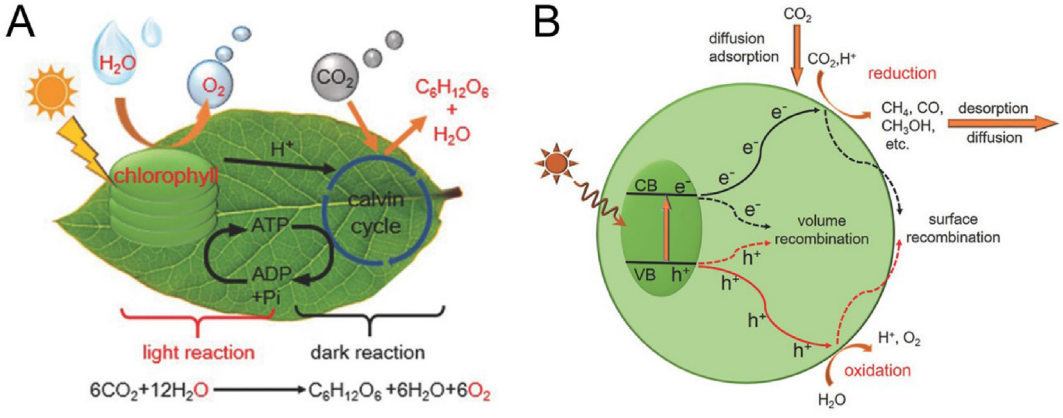

Fig. 1. Scheme of CO_2 reduction process: (A) natural photosynthesis system; (B) photocatalytic system. Reproduced with permission from Wu et al. [4]. Copyright 2017, John Wiley & Sons, Inc.

consequence, engineering the band structures of photocatalysts to an ideal bandgap (about 1.8–2.0 eV) would significantly promote the light absorption efficiency for CRR due to the absorption on the visible light region, which constitutes most of the solar spectrum [4]. Charge separation (step ii) includes the spatial separation of photogenerated electrons and holes, as well as their migration from the bulk to the surface of photocatalysts. The main obstacle of this process is the recombination of electrons and holes at both the bulk and surface. The two competitive factors are the generation rate and the recombination rate of the charge pairs. Recombination would cause a significant loss of free electrons in the CB for CO_2 reduction, which generates heat as non-radiative decay or another wavelength photon via photoluminescence. Therefore, suppressing the recombination of photogenerated electrons and holes and improving their generation rate are of great importance for improving the overall photocatalytic efficiency. Surface reactions (step iii) involve the surface reduction of CO_2 molecules by photogenerated electrons, coupled with water oxidation by photogenerated holes. Similar to all heterogeneous catalytic reactions, the surface reduction of CO_2 on photocatalysts contains three stages, i.e., CO_2 adsorption, redox reactions (electron transfer), and product desorption. CO_2 adsorption is the prerequisite for the subsequent redox reaction process, namely the electron transfer from the photocatalyst to the CO_2 molecule. Redox reactions mainly involve the CO_2 reduction and water oxidation reactions. After the reduction of CO_2, the product desorption is also vital for the whole photocatalytic process because those products may occupy the active site and terminate the following reaction, namely catalyst poisoning. Thus, the reaction conditions and catalyst structure should be carefully designed to ensure the rapid and strong adsorption of CO_2 molecule, quick electron transfer from the catalyst to CO_2 molecules, as well as timely desorption of reduced products.

$$CO_2 + e^- \rightarrow CO_2^{\bullet -} \quad E^0_{redox} = -1.90V\ (NHE) \tag{1}$$

$$CO_2 + 2H^+ + 2e^- \rightarrow HCOOH \quad E^0_{redox} = -0.61V\ (NHE) \tag{2}$$

$$CO_2 + 2H^+ + 2e^- \rightarrow CO + H_2O \quad E^0_{redox} = -0.53V\ (NHE) \tag{3}$$

$$CO_2 + 4H^+ + 4e^- \rightarrow HCHO + H_2O \quad E^0_{redox} = -0.48V\ (NHE) \tag{4}$$

$$CO_2 + 6H^+ + 6e^- \rightarrow CH_3OH + H_2O \quad E^0_{redox} = -0.38V\ (NHE) \tag{5}$$

$$CO_2 + 8H^+ + 8e^- \rightarrow CH_4 + H_2O \quad E^0_{redox} = -0.24V\ (NHE) \tag{6}$$

$$2H^+ + 2e^- \rightarrow H_2 \quad E^0_{redox} = -0.41V\ (NHE) \tag{7}$$

2.2. Critical pathways of photocatalytic CO_2 reduction

The pathways here mainly refer to step iii in the photocatalytic processes, i.e., the surface reduction of CO_2 molecules. As mentioned earlier, the adsorption of CO_2 molecule on the surface of photocatalysts is the first step, which could generate a partially charged species $CO_2^{\delta -}$. The surface-adsorbed CO_2 molecule has three main coordination structures, including oxygen coordination, carbon coordination, and mixed coordination (Fig. 3) [18]. The different binding modes of surface CO_2^- may lead to different reaction pathways. For example, monodentate binding by C atom on the Lewis base centers promotes the formation of the carboxyl radical (COOH)•. Bidentate binding by two O atoms in the oxygen coordination favors the generation of formate anion by preferring the attachment of H to the carbon of CO_2^- [19].

After the adsorption on the surface of photocatalysts, the CO_2 molecule would obtain the first electron and then be transformed into bent $CO_2^{\bullet -}$ anion radical (Eq. (1)). This single-electron reduction reaction of the CO_2 molecule needs a strongly negative electrochemical potential of 1.9 V vs. NHE. Almost no known semiconductor could provide sufficient potential to overcome such a great overpotential (Fig. 2). Thus, this single-electron reduction step is highly unfavorable and identified as the rate-determining step (RDS) [16]. Fortunately, under the assistance of proton, the overpotential values could be reduced, thus facilitating the electron transfer [16]. For instance, as shown in Eqs. (2)–(7), the overpotentials of the formation of formic acid, carbon monoxide, formaldehyde, methanol, and methane are much smaller than that of $CO_2^{\bullet -}$. However, photocatalytic CO_2 reduction (CRR) is a multi-electron transfer process. Although CRR has comparable and even a lower thermodynamically barrier than that of two-electron HER, the CO_2 reduction kinetics is substantially more sluggish. This is because the kinetics of CO_2 reduction reaction prefers a series of elemental one-electron steps rather than the concerted multi-electron transfer processes. Hence, the design of catalysts is needed to surpass HER and promote the CRR process.

After conquering the most difficult step, i.e., the first one-electron reaction, the surface-bound $CO_2^{\bullet -}$ will go through a series of proton-coupled electron transfer steps and transform into various intermediates and respective final products. Although the exact mechanistic details of CO_2 reduction are still not fully elucidated, the pathways of the formation of methane proposed in the literature have been widely accepted [20]. As presented in Fig. 4, they are referred as the (i) formaldehyde pathway, (ii) carbene pathway, and (iii) glyoxal pathway, corresponding to their unique intermediates produced.

2.3. Mechanism of electrocatalytic CO_2 reduction

Electrocatalytic CO_2 reduction technology has shown a great potential in converting CO_2 into value-added chemicals. It has several unique merits: (i) mild and controllable reaction condition (applied potential, reaction temperature, supporting electrolytes,

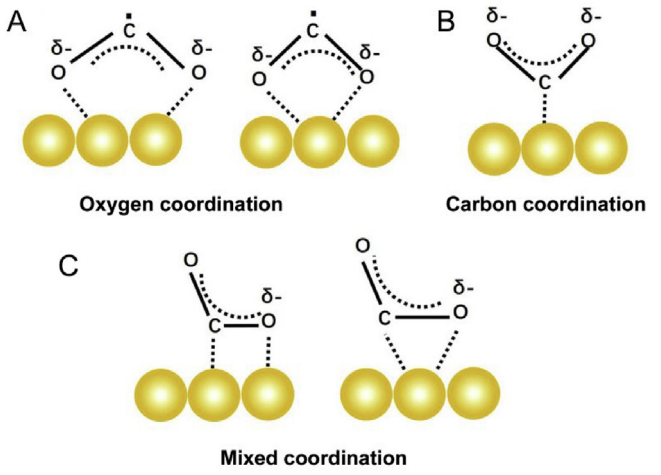

Fig. 3. Three main coordination structures of adsorbed CO_2 molecule on the surface of photocatalysts: (A) oxygen coordination, (B) carbon coordination, and (C) mixed coordination. Reproduced with permission from Fu et al. [10]. Copyright 2019, Elsevier Ltd.

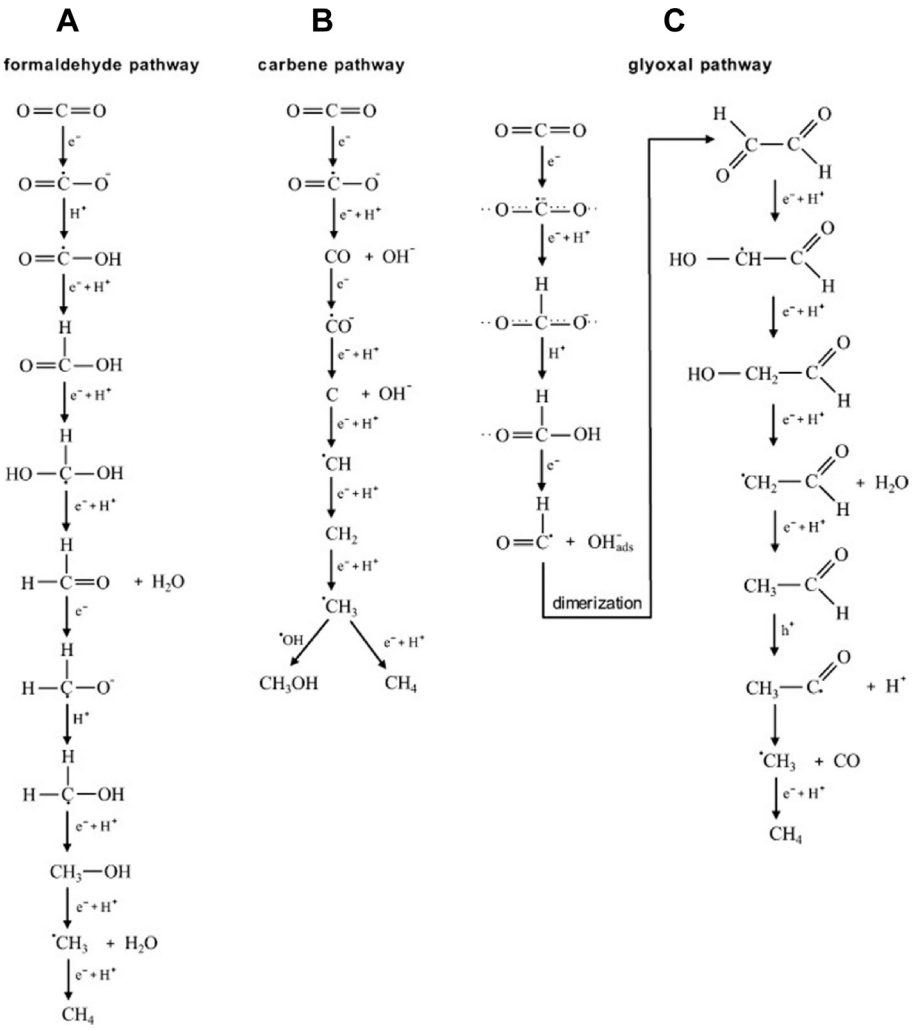

Fig. 4. Three proposed mechanisms for CO_2 reduction: (A) formaldehyde pathway, (B) carbene pathway, and (C) glyoxal pathway. Reproduced with permission from Habisreutinger et al. [16]. Copyright 2013, John Wiley & Sons, Inc.

etc.), (ii) easy for scale-up applications, and (iii) cheap and renewable driving force [21,22]. As mentioned earlier, the major difference between electrocatalysis and photocatalysis is the energy input, and the electrocatalysis is solely driven by electrical energy. The applied electric potential, as well as electric current, can be easily tuned, resulting in a controllable productivity and product selectivity. Therefore, electrocatalytic CO_2 reduction technology is thought to be the closest one to the scale-up and commercial applications among all CO_2 conversion technologies [7]. The electrocatalytic CRR process is very similar to the surface reaction process in the photocatalytic CO_2 reduction [4]. Typically, the CO_2 molecules are first adsorbed at the active site of electrocatalyst and then transformed into various oxygenates and hydrocarbons and finally desorbed from the active site [1]. Owing to the high oxidation state of the CO_2 molecule, CO_2 can be reduced into a variety of oxygenates and hydrocarbons through multiple electron transfer processes. Similar to that in the photocatalytic CRR process (Eqs. (1)–(7)), a variety of half-reactions can also occur with different electrode potentials during the electrocatalytic CRR process, producing diverse hydrocarbon fuels [21].

2.4. Critical pathways of electrocatalytic CO_2 reduction

On the surface of solid-state catalysts, electrocatalytic CO_2 reduction is completed through the interactions between the adsorbed CO_2 molecule and multiple electrons as well as protons from the electrolyte. Apart from the catalyst itself, the experimental parameters, such as applied potential, electrolyte, CO_2 pressure, etc, may also affect the reaction pathways and result in different product distribution. Five most common C_1 products are usually detected in the electrochemical cell, i.e., CO, HCOOH, HCHO, CH_3OH, and CH_4. As schemed in Fig. 5, the products are dependent on the number of electrons transferred to the adsorbed CO_2 molecule [1]. Besides the C_1 product, high-grade C_{2+} products can also be synthesized from the electrocatalytic CO_2 reduction reaction. As summarized in Fig. 6, seven different C_2 and C_3 products can be formed through three typical different reaction routes [20]. In general, the multicarbon products are formed through the dimerization or coupling of different initial C_1 intermediates. To fulfill this process, the C_1 intermediates need to be strongly adsorbed on the surface at a high coverage to ensure the interactions between adjacent activated intermediates. This needs to overcome extra energy barriers related to the catalyst's morphological and electronic characteristics [23]. Besides, the intermediates usually also play a critical role, as shown in Fig. 6. Typically, C_2H_6 and CH_3COO^- are formed from *COH, while $C_2H_2O_2$ and $C_2H_6O_2$ are produced from *CHO intermediate. Meanwhile, the C_2H_4, C_2H_5OH, and n-C_3H_7OH are usually generated through the dimerization of *CO [20]. Owing to the coexistence of those parallel competing pathways, it is highly likely that a mixture composed of various products

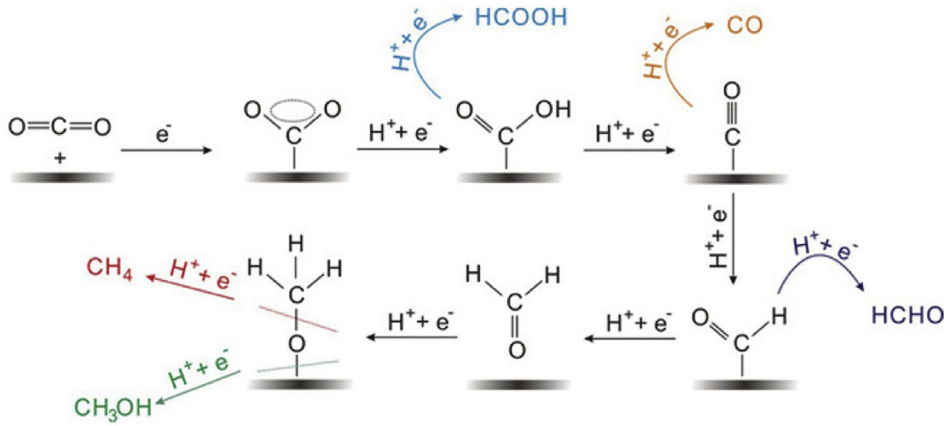

Fig. 5. The pathways for the five main C_1 products of electrocatalytic CRR. CRR, CO_2 reduction reaction. Reproduced with permission from Zhang et al. [1]. Copyright 2017, John Wiley & Sons, Inc.

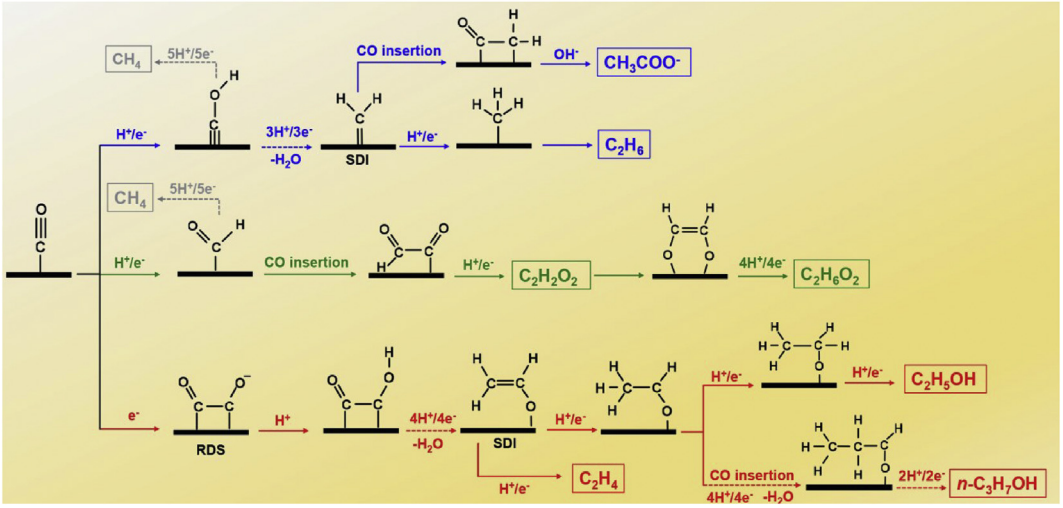

Fig. 6. Most possible pathways for the multicarbon products from *CO on Cu surfaces. Green, blue, and red paths are for trace, minor, and major C_2 products, respectively; gray paths are for C_1 product; dashed arrows mean the multiple consecutive electron/proton transfer steps. Reproduced with permission from Zheng et al. [20]. Copyright 2019, American Chemical Society.

would be produced in the reaction cell. This brings about great technological challenges for increasing the reaction selectivity. Thankfully, the recent mechanism studies have given some clues for changing the selective CO_2 reduction. For the first path in Fig. 6, the formation of both C_2H_6 and CH_3COO^- needs the generation of $*CH_2$ intermediate, while the formation of CH_4 does not need it [24,25]. Thus, the yield of C_2 products can be greatly improved by enhancing the formation of $*CH_2$ intermediate, also called the selectivity-determining intermediate (SDI). In the second path in Fig. 6, both $C_2H_2O_2$ and $C_2H_6O_2$ are derived from the *CHO, which is also a common precursor toward CH_4. However, this route is preferable to produce CH_4 rather than the C_2 products, owing to the low barrier for C_1 product. In the third path, the initial C—C coupling through *CO dimerization is widely taken as the RDS for the entire pathway. After a series of proton-coupled electron transfer steps, the $*CH_2CHO$ intermediate will serve as the SDI for the production of C_2 products [26,27]. The energy barrier of C_2H_5OH formation from $*CH_3CHO$ was calculated to be higher than that of $*CH_2CHO$ reduction into C_2H_4 [28]. This may be the reason of experimentally observed higher selectivity for C_2H_4 over C_2H_5OH on bulk Cu surfaces. Moreover, the selectivity of C_2H_5OH and C_2H_4 also can be reversed through tuning the intermediate binding energy and steering the post-C—C coupling, which promotes C_2H_5OH formation and suppresses C_2H_4 formation [29,30]. As for the formation mechanism of the C_3 product, the C_1—C_2 coupling step may move the reaction forward, while this finding is still inconclusive.

3. Main strategies toward selective multicarbon products

3.1. Main strategies toward selective multicarbon products in photocatalysis

The complex multistep multielectron transfer processes of photocatalytic CO_2 reduction reaction greatly increase the difficulty of tuning the products selectivity. Every elementary step plays an important role in the reaction processes and affects the final products. In the following part, we will introduce and discuss about these main strategies toward selective multicarbon products, in accordance with the three principal steps of the photocatalytic CO_2 reduction processes.

3.1.1. Light absorption

Light is the only energy input to the photocatalytic CO_2 reduction system. Its photon energy and light intensity directly affect the

reaction. Photon energy, represented by the wavelength of incident light, and the bandgap of semiconductor-based photocatalysts decide the thermodynamic barrier of the photocatalytic reaction, whereas light intensity, indicated by the number of photons, and the number of photogenerated charge carriers are the key factors to study the kinetics of the reaction.

As one of the widely studied semiconductors, TiO_2 with a wide bandgap of 3.2 eV can only absorb the ultraviolet light irradiation ($\lambda < 400$ nm), which just accounts for 2–5% of the entire solar spectrum. This greatly limits the utilization of solar spectrum [17]. To resolve this problem, Billo et al. [31] modified the oxygen vacancy–rich TiO_2 ($Ni/TiO_{2[Vo]}$) with some Ni clusters through a simple hydrothermal- and hydrogenation-assisted process. Based on both experimental and computational studies, they found that the formation of Ni nanoclusters and oxygen vacancy in $Ni/TiO_{2[Vo]}$ could enhance light harvesting via a reduction of the optical bandgap with the creation of mid-gap states. In addition, regulating the bandgap also increases the lifetime of electron-hole pairs by suppressing the recombination (Fig. 7A) [31]. As a result, the $Ni/TiO_{2[Vo]}$ exhibits a nearly 100% photocatalytic selectivity toward CH_3CHO, as well as a high activity of 1.76 mmol/g_{cat}, with the irradiation of 300-W halogen lamp under ambient condition (Fig. 7B) [31]. Both the activity and selectivity of the $Ni/TiO_{2[Vo]}$ are much better than those of control samples (Fig. 7C) [31]. Although the researchers failed to directly observe the detailed reaction mechanism of tuning selectivity using their photocatalysts, they speculated that the more negative CB position of $Ni/TiO_{2[Vo]}$ (−1.3 V vs NHE) may be a primary cause (Fig. 7D and E) [31].

To overcome the low light adsorption ability of TiO_2, Lee et al. [32] extracted the light-harvesting complexes (LHCII) from spinach leaves through isoelectric focusing (IEF) and then decorated the LHCII on the surface of Rh-doped TiO_2 (TiO_2:Rh). The obtained hybrid catalyst could not only absorb visible light but also significantly enhance the yield of acetaldehyde. Phongamwong et al. [33] loaded chlorophyll in Spirulina onto the visible light–reactive N-doped TiO_2 (N–TiO_2) catalysts. They found that the photocatalytic stability and C_{2+} (C_2H_4 and C_2H_6) product selectivity were significantly improved after the addition of Spirulina [33]. They claimed the improvement of C_{2+} product selectivity was caused by the increase of photogenerated electrons from chlorophyll in Spirulina. They also proposed a mechanism of chlorophyll in the photocatalysis processes, as illustrated in Fig. 8. Chlorophyll (chl) is first activated to an excited singlet state (^{1}chl*) from a ground state after exciting an electron under illumination. At the same time, the excited singlet state (^{1}chl*) may undergo intersystem crossing (ISC) to their triplet states (^{3}chl*). The excited-state chlorophyll (^{1}chl*, ^{3}chl*) can readily transfer an electron to TiO_2 while simultaneously being converted into its cationic form (chl^+). The chl^+ can decay to the ground-state chlorophyll (chl) after receiving electrons or reacting with some decomposed compounds in Spirulina. Meanwhile, electron-hole pairs are created on the surface of N–TiO_2 under illumination. For the formation of hydrocarbon products, the CO_2 molecule first obtains an electron to form CO_2^- and then combines with a hydroxyl radical (OH) into HCO_3^-. The HCO_3^- would further obtain an electron to form C(ads)• radicals, which could react with H• radicals and convert into different hydrocarbon products, including CH_4, C_2H_4, and C_2H_6 [33]. Apart from utilizing the pristine chl into photocatalysis, Wu et al. [34] extracted the chl from silkworm excrement and then substituted the Mg^{2+} cations in the center of the porphyrin of chl with Cu^{2+}. After modifying with graphene, the composite catalyst only produced C_2H_6 during the 18-h photocatalytic reaction. The authors attributed the high C_2H_6 selectivity to the Cu^{2+} substitution in the chlorophyll, which could promote the transformation of photogenerated electrons due to the suitable energy levels of Cu^{2+}-substituted chlorophyll [34]. In addition, the modification of graphene was found to not only greatly facilitate the photogenerated electrons transformation process through reducing resistance but also stabilize the critical intermediates for C_2H_6 production [34].

Different from the traditional semiconductor photocatalysts, silver halides (AgX, X = Cl, Br, I) have also shown a great potential in photocatalysis because of their unique localized surface plasmon

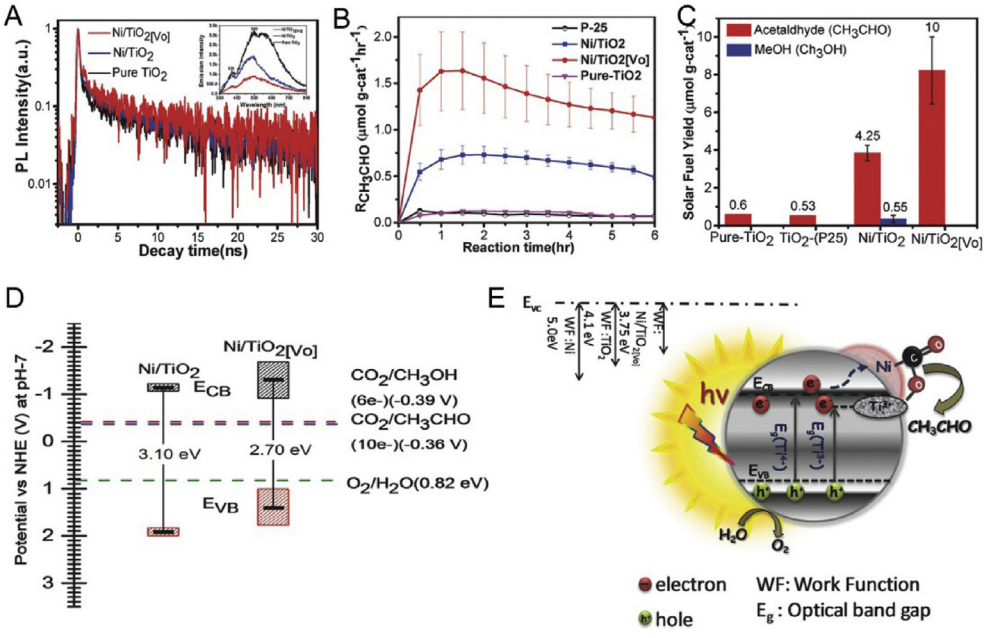

Fig. 7. (A) Time-resolved photoluminescence spectra (inset: PL spectra) of different samples; (B) the acetaldehyde formation rate of different samples; (C) total solar fuel yield of different samples under irradiation of halogen lamp for 6 h; (D) band-edge positions; (E) proposed photocatalytic CRR mechanism on $Ni/TiO_{2[Vo]}$. CRR, CO_2 reduction reaction; PL, photoluminescence; NHE, normal hydrogen electrode. Reproduced with permission from Billo et al. [31]. Copyright 2018, John Wiley & Sons, Inc.

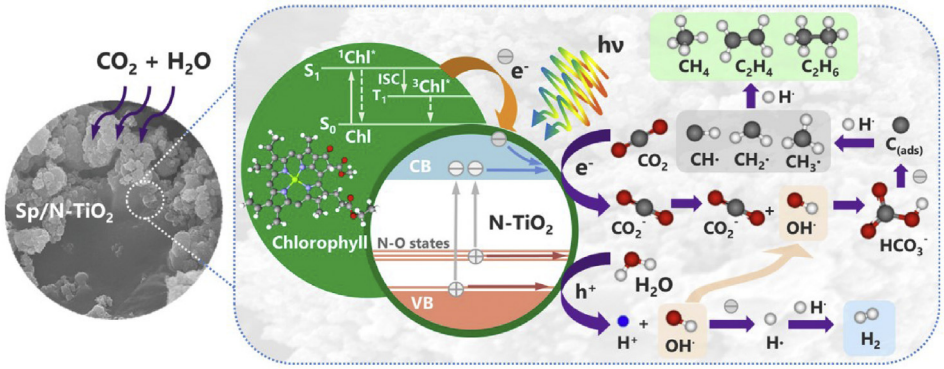

Fig. 8. Proposed photocatalytic CRR mechanism on Spirulina-modified N–TiO_2 catalyst. CRR, CO_2 reduction reaction. Reproduced with permission from Phongamwong et al. [33]. Copyright 2015, Elsevier B.V.

resonance (LSPR) and the favorable bandgap [35–38]. Cai et al. [39] found that tuning the halogen ratio of the $AgCl_xBr_{1-x}$ alloys will have a greater influence on its CB level rather than the VB level. To be specific, both the VB and CB of the $AgCl_xBr_{1-x}$ alloys are composed of Cl 3p, Br 4d, and Ag 4d states, whereas the Ag 4d state contributes little to the composition of the CB [39]. Moreover, Cl 3p and Br 4d levels are lower than the Ag 4d level in the conduction region, which means that the Cl 3p and Br 4d levels are more positive than the Ag 4d level with respect to the vacuum level [39]. Therefore, they introduced some Br in to substitute the Cl in AgCl, which led to the increase in density of states and a downshift of the conduction band minimum (CBM) and subsequently narrows the bandgap. $AgCl_{0.75}Br_{0.25}$ with the optimum CB levels for the electronic coupling between the CB of AgX and Ag exhibited the highest photocatalytic activity with methanol and ethanol yields of 181 and 362 μmol/g, respectively [39]. The high activity should be partly ascribed to the small bandgap value of $AgCl_{0.75}Br_{0.25}$, which augments the incident light absorption. In addition, the LSPR of Ag^0 species also contributes to the light enhancement through the amplified electric field. Apart from the AgClxBr1x alloys, Cai et al. [40] continued their study on the Ag/AgCl system. To improve the optical absorption ability, they designed a kind of red Ag/AgCl photocatalyst, which obtains a large improvement in visible light harvesting. The enhancement of optical absorption was found not only to be attributed to the synergy of Ag and AgCl but also to be ascribed to the Mie scattering effect owing to the distinct morphology. As a result, the methanol and ethanol yields for the red Ag/AgCl samples were measured as 146 and 223 μmol/g, both of which are higher than those of normal AgCl materials (106 and 163 μmol/g for methanol and ethanol, respectively) [40].

Usually, the catalysts are dispersed in the reaction medium or support in the photocatalytic test, which weakens the light absorption of catalysts. To resolve this issue, Nguyen et al. designed an optical fiber photoreactor to enhance the absorption of ultraviolet A (UVA) and ultraviolet C (UVC), thereby enhancing the photocatalytic CO_2 reduction reaction [41,42]. In that system, these optical fibers coated by Cu–Fe/TiO_2 catalysts could flexibly assemble in the reactor. Thus, the UV light can enter along the fibers to conduct the photocatalytic reaction on its surface (Fig. 9). This reactor greatly promoted light absorption by increasing the contact area between light and catalysts. Moreover, the light intensity can be well regulated through the amount of assembled fibers. Typically, when the number of optical fibers increased from 117 to 450, the ethylene production rate also increased from 0.28 to 0.57 μmol/g/h [41]. In addition, the production rate of ethylene of Cu–Fe/TiO_2 catalysts coated on an optical fiber carrier was found to be one order of magnitude higher than that of the same catalyst on the glass plate support [41].

3.1.2. Charge separation

Considering the intrinsic multielectron reaction mechanism, the density of photogenerated electrons on the surface can dynamically affect the rate of every elementary reaction and influence the overall reaction selectivity. The density of photogenerated electrons on the surface largely depends on the relative generation and recombination rates of the photogenerated electrons and holes. Hence, to improve charge separation efficiency, increasing the generation rate as well as suppressing the recombination rate of electron and hole pairs would be an effective approach to control the product selectivity.

During the photocatalysis processes on traditional semiconductor photocatalysts, the wavelength requirement of incident light is usually determined by the semiconductor's bandgaps. Thus, the product selectivity seems to be hardly adjusted by the light excitation attributes. However, the plasmonic metals exhibit totally different light absorption and excitation modes compared with the semiconductor-based photocatalysts. Plasmonic metals, such as Au, Ag, and Cu, can exhibit strong visible-spectrum absorption and intense light focusing at the nanoscale through the unique LSPR, namely the collective free electron oscillations excited by light irradiation [43]. Under the assistance of effective hole scavenger, those LSPR-generated energetic (hot) electrons will accumulate on the plasmonic metals' surface and participate in the CO_2 reduction reactions. The surface distribution of those hot electrons can be greatly affected by the energy and density of the incident photons. Thus, the reaction pathways and rates, toward product selectivity, can also be tuned by the light excitation attributes. Based on this principle, Yu et al. [44] found that the C_2 and C_1 selectivity of photocatalytic CO_2 reduction on plasmonic Au NPs can be well tuned by the light excitation attributes. Higher photon energies (wavelength) and flux (light intensity) promote the simultaneous harvesting of multielectrons from the photo-activated plasmonic Au catalyst, inducing the C–C coupling for C_2 production. Typically, both the excitation wavelength and light intensity significantly affect the product selectivity toward C_2H_6 (Fig. 10) [44]. Under a fixed intensity of 150 mW cm^{-2}, C_2H_6 can hardly be generated if the excitation wavelength was higher than 490 nm [44]. With the fixed excitation wavelength of 488 nm, C_2H_6 can be produced when the light intensity was higher than 300 mW cm^{-2} [44]. However, if the excitation wavelength was fixed at 532 nm, there is not any C_2H_6 formed even if the light intensity was high up to 750 mW cm^{-2} [44]. These results indicated that the C_2 product selectivity in

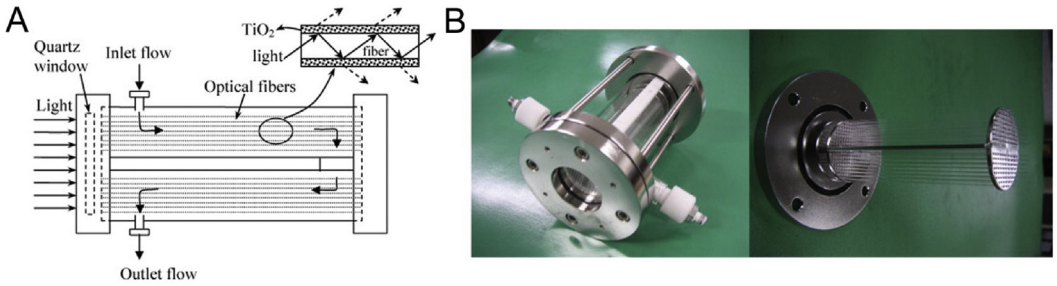

Fig. 9. (A) Scheme of the optical fiber photoreactor; (B) photographs of the photoreactor with the catalyst-coated optical fibers. Reproduced with permission from Nguyen and Wu [41]. Copyright 2007, Elsevier B.V.

photocatalytic CO_2 reduction reactions can be well controlled by the light excitation characteristics of the plasmonic photocatalyst.

Similarly, Tu et al. [45] also found that the plasmonic characteristic of Au in the Au@TiO_2 yolk-shell hollow spheres can create a local electromagnetic field to enhance the generation of electron-hole pairs and remit the charge-carrier recombination in the photocatalytic system. As a result, the Au@TiO_2 yolk-shell hollow spheres not only promote a higher photoreduction yield of CO_2 (the product rate of CH_4: 2.52 μmol/g/h) but also accelerate multiple e^-/H^+ reactions to realize the C—C couple reaction to generate more valuable high-grade carbon species (the product rate of C_2H_6: 1.67 μmol/g/h) under UV-visible light irradiation [45]. To further understand the critical role of LSPR-induced local electric field in the photocatalytic process, the three-dimensional (3D) finite difference time domain (FDTD) simulation was performed to calculate the spatial distribution of enhanced electric field intensity from Au NPs as a function of distance [45]. As shown in Fig. 11, the plasmonic Au NP could effectively couple light from the near field at the TiO_2 surface. Typically, the electric field strength greatly enhanced when it was close to Au NP. Therefore, the concentration of photo-induced electron-hole pairs in the TiO_2 shell near the Au would largely increase. This further intensely speeds up the generation rate of the •CH_3 radical from CO_2 reduction in a certain spacing range between TiO_2 and Au. Under this condition, the •CH_3 radicals would be explosively accumulated on the TiO_2 surface and greatly promote the dimerization process, resulting in the C—C coupling and subsequent generation of C_2H_6.

Graphene oxide (GO) is an attractive low-cost, two-dimensional, atomically thin sheet, which has been widely applied in different areas [46—48]. Owing to the various oxygenated functional groups and stoichiometric C/O ratio on the basal plane, GO can exhibit some wide-bandgap semiconductor-like characteristics [49,50], which makes it a promising potential photocatalyst. Hsu et al. [51] demonstrated that GO could reduce CO_2 to methanol under solar irradiation by modulating the oxygenated functional groups. Later, the same group found that the GO with modification of Cu nanoparticles (NPs) (Cu/GO) can even selectively catalyze the CO_2 reduction into high-grade acetaldehyde under visible light [52].

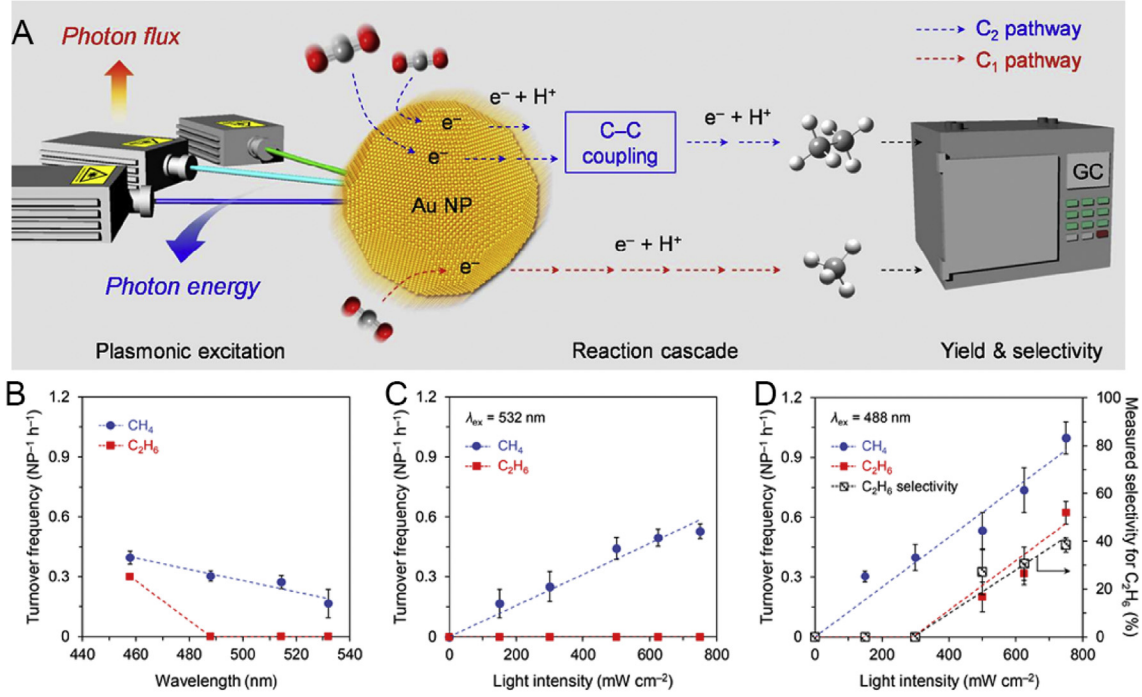

Fig. 10. (A) Scheme of the CO_2 reduction into hydrocarbons under plasmonic excitation with Au NPs catalyst; (B) the relationship between the turnover frequencies for CH_4 and C_2H_6 products and the laser excitation wavelength under a fixed intensity of 150 mW cm^{-2}; (C) the relationship between the turnover frequencies for CH_4 and C_2H_6 products and the light intensity for intraband excitation (λ_{ex} = 532 nm) of Au; (D) the relationship between the turnover frequencies for CH_4 and C_2H_6 products and the light intensity for interband excitation (λ_{ex} = 488 nm) of Au. Reproduced with permission from Yu et al. [44]. Copyright 2018, American Chemical Society.

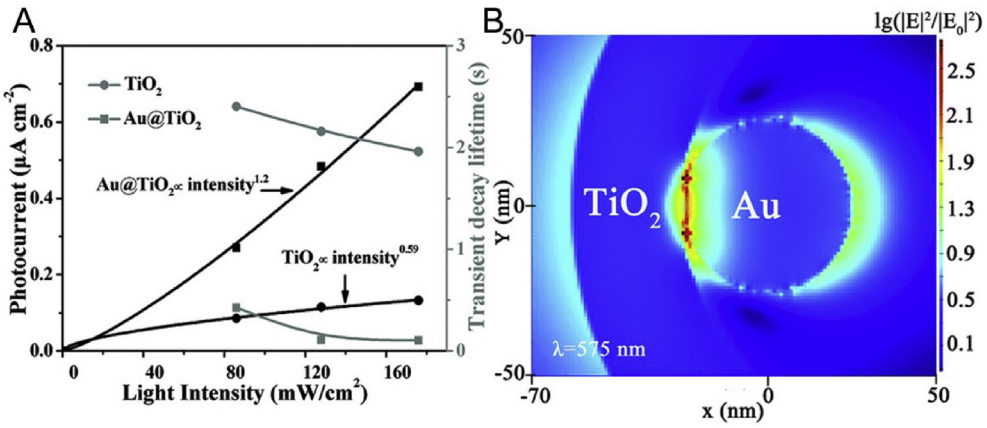

Fig. 11. (A) The responses of photocurrent and transient decay lifetime of surface trap states of TiO_2 and Au@TiO_2 to the light intensity; (B) the spatial distribution of local electromagnetic field enhancement on the x−y plane for Au@TiO_2 yolk-shell nanostructure from an FDTD simulation. FDTD, finite difference time domain. Reproduced with permission from Tu et al. [45]. Copyright 2015, The Royal Society of Chemistry.

After the optimization of the Cu content, the Cu/GO-3 sample showed near-100% selectivity toward acetaldehyde. This high C_2 selectivity may be ascribed to the CB position in Cu/GO-3 slightly lower than the standard reduction potential of CO_2/CH_3OH (−0.38 V vs. NHE, Eq. (5)), thus preferentially producing acetaldehyde (standard reduction potential of −0.36 V vs. NHE) [52]. In addition, the photocatalytic methanol reforming may also further reduce methanol production in the presence of Cu NPs as the lower splitting energy of methanol was relative to that of water [52]. That study suggested the critical role of Cu cocatalyst in tuning the photocatalytic CO_2 reduction selectivity through the suppression of electron-hole pair recombination, the reduction of GO's bandgap, and the modification of work function of GO.

To shorten the charge transport distance and improve ion diffusion to the photocatalyst, Tahir et al. dispersed the TiO_2 NPs in the interlamination of montmorillonite (MMT), a type of multilayered natural clay [53]. They found that the MMT not only greatly enhanced the photocatalytic performance of TiO_2 but also markedly increased the CO_2 reduction selectivity for high-grade hydrocarbon fuels, including C_3H_8, C_2H_6, C_2H_4, and C_3H_6. They assumed that the MMT could suppress the recombination of photogenerated electrons and holes, yielding a large number of CO intermediate and finally high-grade hydrocarbons.

3.1.3. Surface reactions

After the light absorption and charge separation, the surface reaction is the last step of the whole photocatalysis process. Actually, this surface reaction step is totally an electrochemistry reaction and also very similar to the electrocatalytic CO_2 process. Thus, electrocatalyst-like metal cocatalyst is usually combined with the semiconductor photocatalyst for the surface reaction step. Bai et al. [54] found that the different CO_2 adsorption ability of Pd cocatalyst's (111) and (100) crystal facet greatly affected the photocatalytic selectivity. The better CO_2 adsorption ability of Pd (111) facet greatly promotes the Pd tetrahedrons' photocatalytic selectivity toward CO_2 reduction. In addition, Liu et al. [55] reported that monoclinic $BiVO_4$ powder could lead selectively to ethanol under the condition of high-intensity visible-light irradiation. The reason for the high selectivity toward ethanol may be the strong CO_2 adsorption ability of Bi^{3+} site through the weak Bi—O bond. Thus, the adsorbed CO_2 could efficiently receive the photogenerated electrons from the V 3d-block bands of $BiVO_4$ [55]. Recently, our study shows the different CO_2 adsorption ability on Cu_2O (110) and (100) facets. This leads to the reconstruction of (110) facet and the formation of Cu nanoclusters toward a high selectivity of CO_2 reduction to methanol [56].

Tu et al. [57] reported a TiO_2-graphene 2D sandwich-like hybrid nanosheet structure (G-TiO_2), in which the dispersion of TiO_2 hindered the collapse and restacking of exfoliated sheets of graphene. In addition, the photogenerated electron-hole recombination can be effectively prevented by trapping electrons at the Ti^{3+} sites on the surface. The G-TiO_2 hybrid exhibited a high photocatalytic activity in reducing CO_2 into valuable hydrocarbons (CH_4 and C_2H_6). Interestingly, with graphene, the CH_4 production rate slowly decreased, but the C_2H_6 production rate noticeably increased, i.e., the molar ratio of C_2H_6 to CH_4 increases from 0.71 to 3.04 [57]. This implies that the production of C_2H_6 was favorable with the introduction of graphene. The preferential formation of C_2H_6 may be attributed to the ability of electron-rich graphene in stabilizing the $*CH_3$ species, promoting the dimerization of $*CH_3$ into C_2H_6 and restraining the combination of $*CH_3$ with H^+ and e^- into CH_4 [57]. Later, Wu et al. [58] also found that graphene could improve the porphyrin's photocatalytic CO_2 reduction selectivity toward C_2H_4. During the formation of C_2H_4 from CO_2 reduction, the key step is self-coupling or intercoupling of the radicals. The intermediates with a delocalized electronic structure can receive electrons continuously after attaching to the graphene through the π-π noncovalent bond [58]. Thus, it greatly decreased the potential of the transition states and promoted the coupling of intermediates. Sorcar et al. [59] also found the great role of graphene in promoting ethane selectivity in the photocatalytic CO_2 reduction process. Pt-sensitized graphene-wrapped reduced blue titania (RBT) photocatalyst produces a record high yield of ethane (C_2H_6) and methane through the photocatalytic CO_2 reduction [59]. Under one sun AM 1.5G illumination, approximate totals of 77 μmol/g C_2H_6 and 259 μmol/g CH_4 were produced in a continuous flow cell with a stability as long as 42 h [59]. The systematic ultraviolet photoelectron spectroscopy study indicated that the formation of ethane mainly depended on upward band bending on the RBT/graphene interface [59]. As schemed in Fig. 12A and B, adsorbed CO_2 reacted with the photogenerated electrons accumulated on Ti^{3+} sites, while water was oxidized on the conducting graphene network by the holes migrated from the RBT VB. Furthermore, the graphene could stabilize $*CH_3$ radicals, promoting the ($*CH_3 + *CH_3 \rightarrow C_2H_6$) reactions for ethane generation.

Apart from graphene, Cu NPs also exhibit a similar ability in stabilizing reaction intermediates. Park et al. [60] reported on a sodium trititanate nanotubes (TNTs; $Na_xH_{2-x}Ti_3O_7$)—based ternary

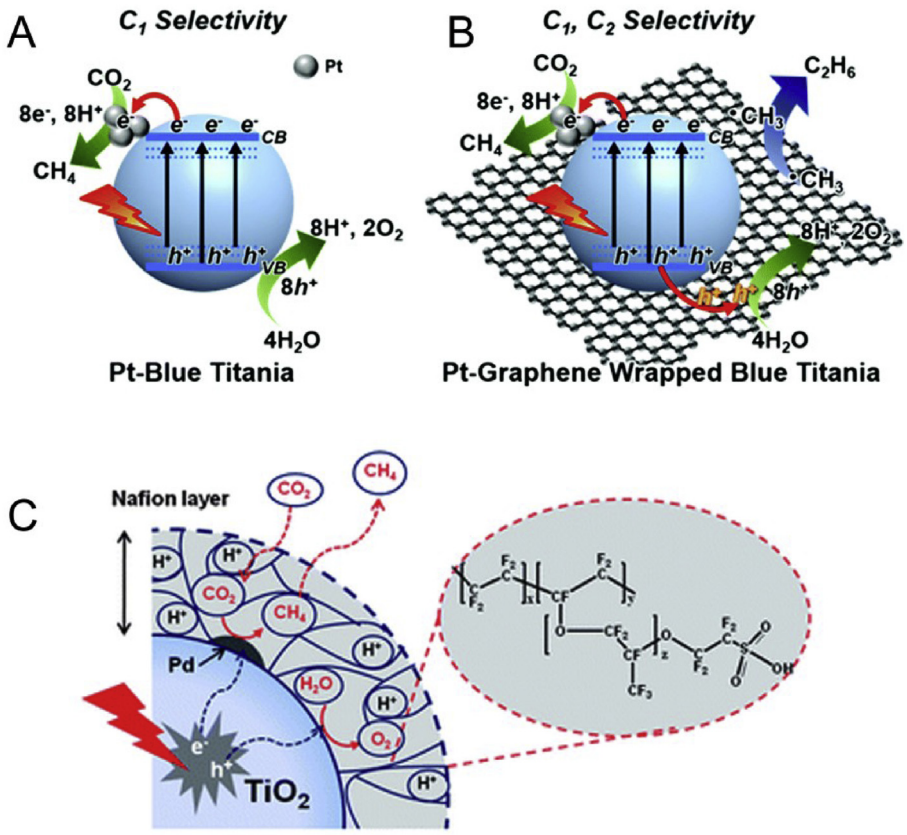

Fig. 12. Scheme of photocatalytic CRR process over Pt-RBT (A), Pt-graphene–wrapped RBT (B) [59], and (C) Nafion layer–coated Pd-deposited TiO_2 nanoparticles. CRR, CO_2 reduction reaction; RBT, reduced blue titania. Reproduced with permission from Kim et al. [62]. Copyright 2012, The Royal Society of Chemistry.

catalyst, in which TNTs were decorated with Cu NPs and CdS quantum dots. Under irradiation with visible light above 420 nm, the ternary photocatalyst could catalyze CO_2 and water into C_1–C_3 hydrocarbons, including CH_4, C_2H_6, C_3H_8, C_2H_4, and C_3H_6 [60]. The Cu NPs may play a major role in transient trapping of methyl radical, which in turn self-reacts to produce ethane [60]. Mao et al. [61] found that the microstructures of photocatalyst also affected the selectivity of CO_2 reduction through stabilizing reaction intermediates. The g-C_3N_4 derived from urea (denoted as u-g-C_3N_4) with mesoporous flake-like structure generated a mixture containing CH_3OH and C_2H_5OH. While the non-porous flaky g-C_3N_4 derived from melamine (denoted as m-g-C_3N_4) could selectively produce C_2H_5OH. The reason for the selectivity difference may be due to the microstructures of g-C_3N_4. The exchange of the formed *OCH_3 or CH_3OH may be hindered by m-g-C_3N_4 owing to the unfavorable non-porous structure. Thus, the possibility of the dimerization of *OCH_3 intermediates into C_2H_5OH would be greatly promoted, resulting in a high C_2H_5OH selectivity.

Kim et al. [62] reported that the Nafion layer coated on the Pd-deposited TiO_2 NPs photocatalyst could also markedly enhance the photocatalytic reduction CO_2 into hydrocarbons (mainly CH_4 and C_2H_2) under UV and solar irradiation conditions, shown in Fig. 12C. The critical role of the Nafion layer was proposed to enhance the local proton activity within the layer to facilitate proton-coupled multielectron transfer (PCET) reactions, to stabilize intermediates, and to inhibit the reoxidation of the CO_2 reduction products [62]. Specifically, the enhancement of local proton activity and various intermediates stability in the Nafion layer facilitated the multielectron transfer processes, resulting in the formation of the multicarbon products.

3.1.4. Photodegradation, hydrocarbon coupling, and inorganic-biological hybrids

Besides the strategies on light absorption, charge separation, and surface reactions toward improving the selective C_2 product formation, the possible photodegradation of produced C_2 products should also be carefully considered and avoided. Hamdy et al. [63] evaluated three strategies to improve the intrinsic photocatalytic performance of Ti sites in silica matrices. First, they incorporated Ti sites in a TUD-1 silica matrix to improve Ti dispersion and adapt the porous structure. Second, ZnO was added to improve CO_2 adsorption capacity when sunlight was not available for reaction. Third, the performance of visible light–sensitive CrO–Ti sites was evaluated. Under the synergy between TiO_x and ZnO NPs as well as TiO_x, not only the apparent CO_2 reduction rates were studied but also the possible following conversion of produced hydrocarbons. They found that the photocatalytic performance of ZnO–Ti-TUD-1 and Cr–Ti-TUD-1 were inferior to the parent Ti-TUD-1 [63]. In addition, the Ti-TUD-1 exhibited the poorest activity in hydrocarbon (i.e., CH_4, C_2H_4, C_2H_6, C_3H_6, and C_3H_8) degradation, while ZnO–Ti-TUD-1 and Cr–Ti-TUD-1 showed very striking degradation rates under the same illumination conditions. Those results showed that the better photocatalytic CO_2 reduction performance of parent Ti-TUD-1 mainly is due to the low photodegradation ability toward the hydrocarbon products. This clearly demonstrated that the hydrocarbon degradation ability should be carefully studied in designing highly effective photocatalyst. Niu et al. reported that the selectivity of photocatalytic CO_2 reduction on g-C_3N_4 could be tuned by the band structure (Fig. 13) [64]. The bulk g-C_3N_4 with a bandgap of 2.77 eV mainly produces acetaldehyde (CH_3CHO), while the g-C_3N_4 nanosheets with a bandgap of 2.97 eV

focuses on generating methane (CH_4) [64]. The favorable formation of acetaldehyde on bulk g-C_3N_4 mainly attributed to the limited oxidation of CH_3CHO due to the weak driving force from the narrow bandgap.

Besides the unfavorable hydrocarbon degradation during the CO_2 reduction processes, the CO_2-involved hydrocarbon coupling reaction may provide an alternative path for CO_2 conversion reaction. Instead of C_1 products, benzyl acetate was produced as the main product over Cu_2O/Cu when coupling benzyl alcohol oxidation with photocatalytic CO_2 reductions [65]. In addition, Li et al. [66] also successfully coupled methane oxidation with photocatalytic CO_2 reduction on Ag/TiO_2 photocatalyst, resulting in the production of CO and C_2H_4 with high yields of 1,149 and 686 μmol/g/h, respectively, under simulated solar irradiation.

Considering the challenges of selectivity on inorganic photocatalyst, the inorganic-biological hybrid system has also been put forward. Our recent work shows a semiartificial photosynthetic system with inorganic-biological hybrid, *Halobacterium* purple membrane–derived vesicles (PMVs)–coated Pd-deposited porous hollow TiO_2 NPs (Pd-HTNPs), could effectively photocatalytic reduce CO_2 [67]. The *Halobacterium* PMVs could not only retain their intrinsic biological function as a proton pump but also acted as a photosensitizer that injects light-excited electrons into the CB of TiO_2 [67]. Similarly, the electrons trapped on Pd cocatalysts and the protons accumulated inside the cytometric architecture are in concert to reduce CO_2 via proton-coupled multielectron transfer processes [67]. Sakimoto et al. developed a hybrid system, by combining the *Moorella thermoacetica* with cadmium sulfide NPs (*M. thermoacetica*-CdS), for photocatalytic CO_2 reduction (Fig. 14A and B) [68]. Owing to the highly efficient light harvesting of CdS NPs and the high catalytic selectivity of *M. thermoacetica*, the self-augmented biological system selectively reduces CO_2 into acetic acid continuously over several days of light-dark cycles with a relatively high quantum yields. Coupling with a TiO_2–Mn(II) phthalocyanine (TiO_2-MnPc) water oxidation photocatalyst, an *M. thermoacetica*-CdS + TiO_2-MnPc tandem system could be constructed for solar-to-chemical production [69]. To further enhance the electron transfer rate, Zhang et al. [70] introduced gold nanoclusters (AuNCs) into the phosphate buffer saline (PBS) as an intracellular and biocompatible light absorber (Fig. 14C and D). Translocation of those AuNCs into the non-photosynthetic bacteria rendered the generation of acetic acid from CO_2 via photosynthesis [70].

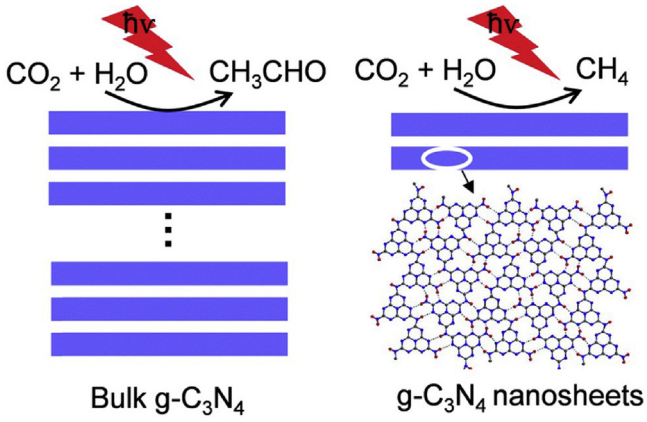

Fig. 13. Scheme of photocatalytic CRR process on bulk g-C_3N_4 and g-C_3N_4 nanosheets. CRR, CO_2 reduction reaction. Reproduced with permission from Niu et al. [64]. Copyright 2014, The Royal Society of Chemistry.

3.2. Main strategies toward selective multicarbon products in electrocatalysis

Based on the aforementioned analysis of the reaction mechanism, two apparent ways exist to improve the multicarbon product selectivity during electrocatalytic CO_2 reduction. One is to stabilize the key intermediate, and the other is to reduce the formation energy barrier of respective multicarbon products. Usually, the electrocatalytic system consists of an external electric field, electrolyte, and electrodes. Thus, it provides three corresponding possibilities to improve the multicarbon product selectivity. The first one is to tune the external electric field by controlling the applied potential in the electrocatalytic CO_2 reduction process [71]. The second one is changing the electrolyte from aqueous solution, organic phase, ionic liquids, or solid electrolyte to regulate the transport of reaction species [56,72]. The last one focuses on the design of the electrodes. Electrodes are the core part of the electrocatalytic CO_2 reduction processes. In general, the electrodes are referred to the working electrode and the counter electrode, which are responsible for the CO_2 reduction and the counter-reactions such as water oxidation, respectively. Although the optimization of the counter electrode may help to improve the overall energy efficiency, its impact on CO_2 reduction selectivity has rarely been reported. Therefore, we only discuss about the aspect of the CO_2 reduction on the working electrode. In addition, considering the critical role of CO intermediate in the production of C_{2+} product during electrocatalytic CO_2 reduction processes, CO has also been taken as the initial reactant to investigate the C_{2+} product formation mechanism [73]. Thus, some work about electrocatalytic CO reduction into C_{2+} product is also included in this review.

3.2.1. Applied potential

During the electrocatalytic CO_2 reduction processes, an external electric field is usually needed to overcome the thermodynamic barrier, namely the overpotential. Thus, different product distribution often appears in different applied potential values. To understand the influence of overpotential on CO_2 reduction mechanism, Peterson et al. [74] conducted a theoretical investigation based on Cu (211) step surface by density functional theory (DFT) combining with a computational hydrogen electrode (CHE) model. Their results showed that $HCOO^-$ and CO were first formed from −0.41 V vs. reversible hydrogen electrode (RHE) and more negative applied potential led to further CO_2 reduction [74]. When the potentials are negative than −0.71 V (RHE), C_2H_4 and CH_4 would be the major products [74]. To further understand the influence of applied potential on the reaction kinetics and product selectivity, Cheng et al. [75] carried out the *ab initio* molecular dynamics simulations in a water/Cu(100) system. When the applied potential (U) is more positive than −0.6 V, the formation of C_2H_4 via the coupling of *CO–CO and *CO–COH is favored over the formation of CH_4 via *CHO, owing to the lower energy barrier (0.69 vs 1.0 eV) [75]. Thus, C_2H_4 is the major product in this potential range. In the range of −0.6 to −0.8 V, the surface coverage of *CO would decrease owing to the competitive adsorption of *H [75]. This resulted in a decrease in the CO dimerization rate and subsequently a reduction of C_2H_4 yield. In other words, the Faradaic efficiency (FE) of C_2H_4 declines, while that of H_2 increases (Fig. 15A). Under more negative potentials than −0.8 V, *CHO would be formed from H* and non-adsorbed CO through an Eley-Rideal (ER) mechanism. This *CHO is the intermediate for the generation of CH_4 and C_2H_4. Thus, both C_2H_4 and CH_4 appeared in this potential window.

Besides the theoretical study, Ren et al. [71] also investigated the role of applied potential in CO_2 reduction. They performed the CO_2 reduction study on four copper electrocatalysts under the potential range of −0.45 to −1.30 V. The selectivity of 20 previously reported

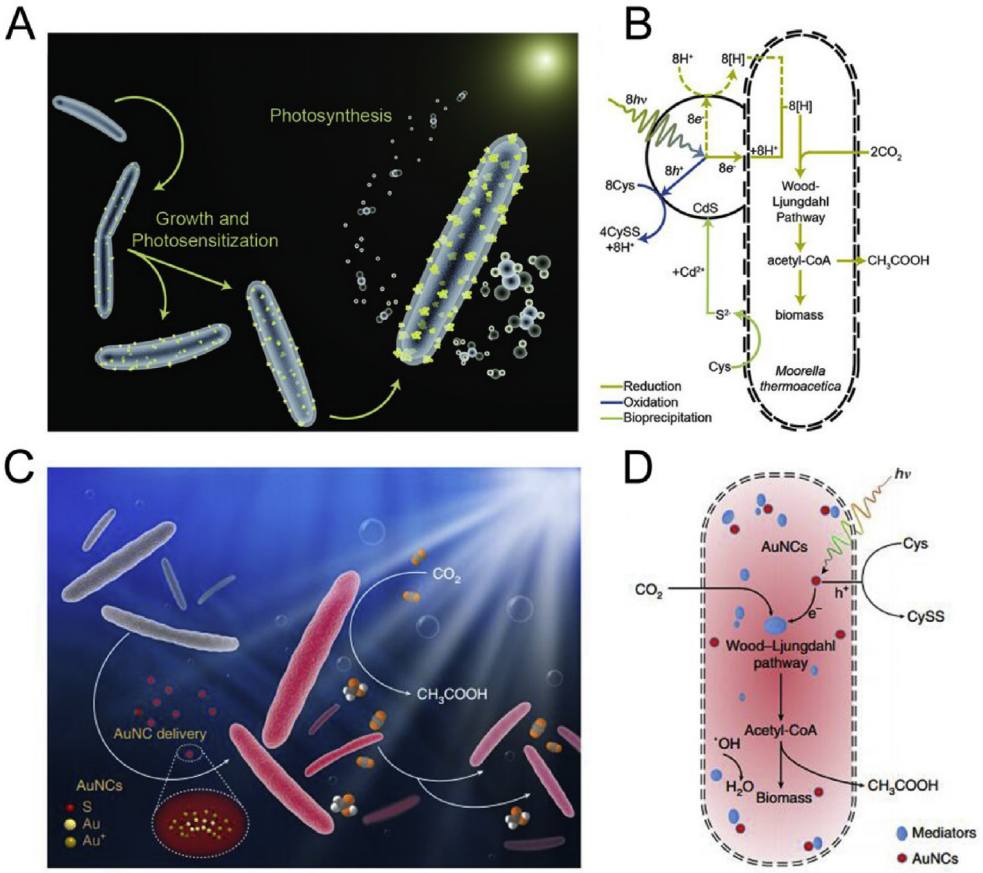

Fig. 14. (A) Scheme of the *M. thermoacetica*-CdS PBS; (B) proposed CRR mechanism of the *M. thermoacetica*-CdS PBS [68]; (C) scheme of the *M. thermoacetica*-AuNC PBS; (D) proposed CRR mechanism of the *M. thermoacetica*-AuNC PBS. CRR, CO_2 reduction reaction. Reproduced with permission from Zhang et al. [70]. Copyright 2018, Springer Nature.

copper catalysts for CO_2 reduction had also been analyzed in their study [71]. As shown in Fig. 15B–E, different products could only be formed in specific potential ranges. Specifically, CO and $HCOO^-$ were significantly formed only when potentials are more positive than −0.7 V, C_2H_4 and C_2H_5OH were generated in great quantities from −0.8 to −1.1 V, and CH_4 was selectively produced at potential more negative than −1.1 V. The aforementioned theoretical and experimental results suggested that applied potential played a crucial role in the selectivity of CO_2 reduction.

3.2.2. Electrolyte

3.2.2.1. H^+/OH^-. Aqueous solution is the most common electrolyte in the electrocatalytic CO_2 reduction because of its controllability and low cost. Generally, the aqueous electrolyte is made up of H^+, OH^-, cation, anion, and H_2O molecules. H^+/OH^- concentration dominates the solution pH value, which is a significant factor for CO_2 reduction reaction. Owing to the acidic gas characteristic of CO_2 molecules, there would be an acid-base equilibrium between dissolved CO_2 and bicarbonate. In other words, the H^+ concentration may be changed owing to the dissolution of CO_2 in H_2O and the ionization of the resulting H_2CO_3. Both CO_2 reduction and the competitive water reduction comprise a series of protonation steps. Thus, H^+ concentration plays a critical role in the product selectivity of the electrocatalytic CO_2 reduction processes. Varela et al. [76] reported that the electrocatalytic activity and selectivity of Cu foil toward CO_2 reduction was greatly influenced by the concentration of the bicarbonate electrolyte. They found that ethylene was selectively formed in the lower concentrated bicarbonate electrolytes, while the high concentrations of bicarbonate favored the production of H_2 and CH_4 [76]. A similar phenomenon had also been observed, which may be attributed to the difference of interfacial pH near the catalyst surface [77]. Specifically, the dissolving of CO_2 would introduce pH change by increasing the H^+ concentration, while the bicarbonate electrolytes with different concentration have different pH buffering capacity. Thus, different local pH near the catalyst surface would appear in the bicarbonate electrolytes with different concentrations and thus resulting in diverse product distribution. Theoretically, Schouten et al. [78,79] also observed that the OH- anions possibly enhance the C_2 selectivity through suppressing HER competition. Thus, a great amount of CO_2 reduction studies have been conducted in the flow cell electrolyzer, which can maintain high pH on the electrode surface and high C_2 selectivity [80–82].

3.2.2.2. Cations. Besides the influence of pH caused by H^+ and OH^-, the cations and anions in the electrolyte may also affect the C_2 product selectivity through tuning the stability of the intermediate [83–85]. Murata and Hori [86] studied the influence of cations on the CO_2 reduction selectivity, including Li^+, Na^+, K^+, and Cs^+. They found that product selectivity was closely related to the size of the cation [86]. Specifically, the large-sized cation favors the formation of C_2H_4, while the small-sized cation tends to promote the generation of CH_4 [86]. This behavior was ascribed to the difference of cationic species that induced outer Helmholtz plane (OHP) potential. Because H^+ is a charged species, its concentration, as well as the pH around the catalyst, would depend on the OHP potential

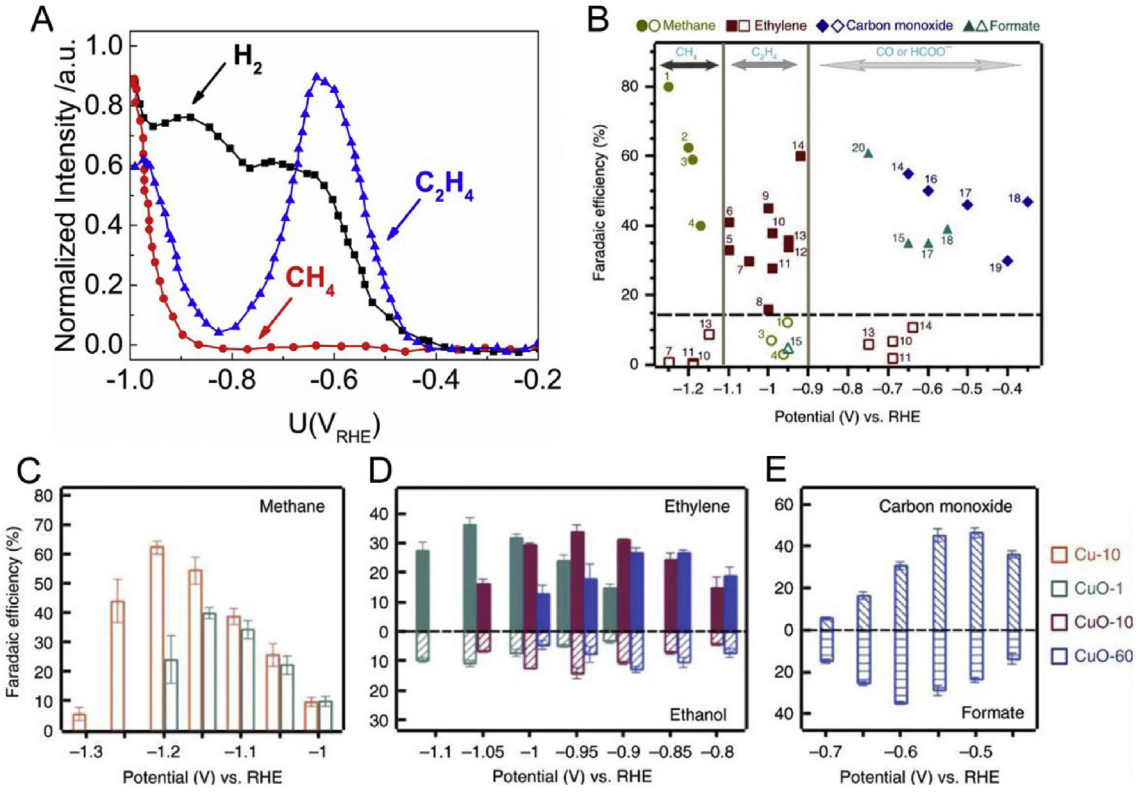

Fig. 15. (A) Experimental mass fragments of C_2H_4, H_2, and CH_4 during electrocatalytic reduction of CO in 0.1 M phosphate buffers (pH 7); reproduced with permission from Cheng et al. [75]. Copyright 2017, National Academy of Sciences. (B) The selectivities of 20 different Cu catalysts reported by 11 different research groups at different applied potentials; (1) isolated particles [153], (2) Cu-10 [71], (3) polycrystalline [115], (4) polycrystalline [154], (5) Cu_2O (3 C cm^{-2}) [155], (6) 44-nm cubes [130], (7) nanoparticles [156], (8) KF roughened Cu [157], (9) electrochemically cycled Cu [158], (10) Cu_2O (1.7 μm) [115], (11) mesocrystals [159], (12) CuO-10 [71], (13) nanocrystals (Cu-NC10) [156], (14) Cu_2O (O_2 plasma 20 min) [110], (15) nanocrystals (Cu-NC20) [156], (16) CuO nanowire [160], (17) CuO-60 [71], (18) Cu_2O (annealing) [161], (19) Cu_2O (11 C cm^{-2}) [155], and (20) CuO nanoparticles [162]. (C) FE of methane over Cu-10 and CuO-1 catalysts at different potentials. (D) FE of ethylene and ethanol on CuO-1, CuO-10, and CuO-60 catalysts at different potentials. (E) FE of carbon monoxide and formate over CuO-60 catalyst at different potentials. FE, Faradaic efficiency; RHE, reversible hydrogen electrode. Reproduced with permission from Ren et al. [71]. Copyright 2018, Springer Nature.

values, thus affecting the product selectivity. In addition, owing to the larger dipole moment of *CO than that of *CHO, the *CO would be more stabilized in the hydrated cations induced electric field, resulting in higher C_2 product selectivity [87]. Montoya et al. [88] also found that a charged water layer on Cu(100) can significantly improve the stability of CO dimer configuration under the presence of cations other than H^+ and thus promote the C_{2+} productivity. This effect can be further explained by the local cation-induced fields. The solvated cations in the double layer can induce a local electric field near the metal catalyst surface and then significantly stabilizes the intermediates [89]. Apart from the alkali metal cations, the multivalent cations in the electrolyte can also influence the product selectivity. Schizodimou and Kyriacou [90] studied the influence of various multivalent cations on the CO_2RR on a CuSnPb alloy electrode, including Na^+, Mg^{2+}, Ca^{2+}, Ba^{2+}, Al^{3+}, Zr^{4+}, Nd^{3+}, and La^{3+}. They found that the presence of La^{3+} greatly promoted the reaction rate compared with that of Na + at the same potential in acidic electrolytes [90]. In the Na^+-containing acidic electrolyte, only CH_3OH (35% FE) and HCOOH (28% FE) were produced. However, the CH_3CHO (17.6% FE) was generated in the Zr^{4+}-containing electrolyte. However, the low solubility of multivalent cations limited their application [8].

3.2.2.3. Anions. Similar to the cations, the anions (especially halides) in the electrolyte also have the ability to adjust the product selectivity. Varela et al. [91] studied the role of halides in the electrolyte, including Cl^-, Br^-, and I^-, in tuning the activity and selectivity of electrocatalytic CO_2 reduction on Cu. They found that the reaction activity and selectivity actually can be tuned by the concentration and nature of the halides in the electrolyte. Huang et al. [84] also investigated the influence of $KClO_4$, KCl, KBr, and KI electrolyte on the CO_2 electroreduction reaction. The formation of ethylene and ethanol was enhanced with the change of electrolyte anion from ClO_4^-, Cl^-, Br^- to I^- [84]. The total FE of C_2 and C_3 products can be up to 74% in the presence of KI [84]. Linear sweep voltammetry suggested that the KI electrolyte promoted the *CO population on the surface, resulting in the favorable formation of C_2 products. *In situ* Raman spectroscopy study showed that the I^- could adjust the coordination environment of adsorbed *CO and accelerate the C—C coupling for the formation of C_2 products.

Besides promoting the C—C coupling of intermediates, anions may also alter the catalyst structure and regulate product selectivity. Kim et al. [92] found that the Cu electrode undergoes a substantial surface reconstruction from a polycrystalline surface to Cu(100) surface by *operando* electrochemical scanning tunneling microscopy (EC-STM) study, during CO_2RR at −0.9 V for 3 h in 0.1 M $KHCO_3$. Their study also showed that such a surface reconstruction was transformed through the intermediate Cu(111) orientation and became faster in 0.1 M KOH (Fig. 16A–C) [8,93]. Gao et al. [85,94] observed that I^- in the electrolyte could cause significant nanostructuring of the plasma-oxidized polycrystalline Cu foils into well-shaped Cu crystals containing stable CuI species, even at an open circuit potential. Different cations (K^+ vs. Cs^+) in the electrolyte could further tune the morphology of the transformed

particles (Fig. 16D–F) [8,85,94]. During the CO_2 reduction processes, the Cs^+ in the electrolyte could avoid further reduction of some smaller CuI particles into Cu particles, while the K^+ cannot [85,94]. Those Cu^+ species in the CuI could facilitate C–C coupling and favor the formation of C_2 products [95]. Furthermore, the size of Cu nanocubes could be tuned by changing the KCl concentration. After the low-pressure plasma pretreatments, Cu nanocubes exhibited an improved selectivity (73% FE) toward C_2–C_3 products. Moreover, the polycrystalline Cu foil surface can also be electrochemically oxidized into $Cu(OH)_2$ nanowires (NWs) through an anodization process in concentrated KOH (Fig. 16G–I) [8,96,97]. Under reduction potentials, $Cu(OH)_2$ NWs can further be reduced into mixed-valence Cu oxide and catalyze CO_2 reduction into ethylene. Similarly, Jiang et al. [98] also developed a metal-ion battery cycling method to tune the facet exposure on Cu foil. The 100-cycled Cu nanocube was mainly (100) facets. Those active (100) facets greatly boosted the C_{2+} production, in which the C_{2+}-to-C_1 product ratio was sixfold that of blank Cu foil, with the highest C_{2+} FE of more than 60% and a corresponding C_{2+} current of more than 40 mA cm^{-2} [98]. Those examples show the critical impact of anions on the electrocatalytic CO_2 reduction selectivity and also exhibit the rich possibilities for catalyst designing via electrolyte-driven nanostructuring.

3.2.2.4. Organic additive. Thevenon et al. [99] reported an organic additive of N,N′-ethylene-phenanthrolinium dibromide (**1-Br$_2$**), which can significantly improve the Cu catalyst's electrocatalytic CO_2 reduction activity (7 mA cm^{-2}) and multicarbon product selectivity (70% FE). Further mechanistic research demonstrated that these enhancements can be attributed to the multiple functions of **1-Br$_2$** additive. Specifically, the **1-Br$_2$** additive could induce the *in situ* production of Cu nanocubes with the selective formation of multicarbon product and stabilize the morphology by depositing an organic film onto the electrode [99]. A proposed work mechanism of **1-Br$_2$** additive is shown in Fig. 17. On a smooth Cu electrode surface, the bromide anions can corrode surface Cu and create nucleation sites for the nanostructuring process. As a result, well-defined nanocubes formed on the Cu surface under the assistance of corrosion enhancement via potentiostatic electrochemical impedance spectroscopy (PEIS) cycles. Under a bias of 1.07 V RHE, the reductive dimerization of phenanthrolinium dication would occur by the coupling of the generated radical (1C–Br) on the surface of Cu, developing a protected organic film onto the electrode [99]. Such an organic film can not only stabilize the morphology of Cu nanocubes but also facilitate the C–C coupling. Notably, surface-protected organic film using **1-Br$_2$** additive is a great advantage than the alkali halide salts. Alkali halide salts can promote a nanostructuring process. But it suffered from a quick structural degradation and decay of performance during electrocatalysis.

3.2.2.5. H_2O

3.2.2.5.1. Aqueous electrolytes. Water is a common solvent in the electrolyte. However, Xiao et al. [100] discovered that the surface-adsorbed water on Cu(111) could serve as a strong proton donor and promote the electrochemical dehydration process which was only involved in the generation of hydrocarbon products, based on their grand canonical quantum mechanics (GC-QM) study. Thus, it could selectively produce hydrocarbon products rather than oxygen-containing alcohol products [100]. Lum et al. [101] performed the CO_2 reduction experiment using $C^{16}O$ as a reacting substance in the isotopically labeled $H_2^{18}O$ electrolyte. They surprisingly found that most of the produced ethanol (60–70%) contained ^{18}O, which indicates water played a dominant role in providing oxygen atoms the product formation [101]. However, Clark et al. [102] thought those experimental observations can be explained by the isotopic scrambling between water (solvent) with transiently produced carbonyl-containing intermediate reduction products. Their theoretical study also demonstrated that the reversible hydration of carbonyl-containing species could facilely appear in the vicinity of the Cu surface [102]. Usually, the interface water layer consists of a loosely packed hydrogen bond network, which is quite different from the bulk water structure [103]. Thus, experimentally, it is a great challenge to study the role of water in C_2 product selectivity. Great effort had been put into the theoretical calculations study. Typically, to improve the rationality of the original CHE model, both explicit and implicit solvation models had been widely introduced to study the dielectric response of surface water molecules layers [103]. The great number of experimental phenomena is consistent with those calculations, which includes explicit/implicit water layers and a dielectric continuum model in real CRR conditions [103]. Those calculation studies provide an important benchmark for future experimental investigation.

3.2.2.5.2. Non-aqueous electrolytes. Despite the progress made with aqueous solvent, the efficient and selective electrocatalytic CO_2 reduction remains challenging, owing to the limited solubility of CO_2 in water. CO_2 could dissolve in water with a concentration of about 33 mM at 25 °C and 1 atm. This significantly restricts the CO_2 diffusion, reduction rate, and selectivity [8]. Furthermore, the ubiquitous competitive HER hinders the CO_2 reduction. Alternatively, some non-aqueous electrolytes have also been developed for electrocatalytic CO_2 reduction, such as organic solvent of acetonitrile, methanol, and N,N-dimethylformamide, as well as ionic liquid [72]. CO_2 can be well dissolved in these non-aqueous electrolytes, with several-folds higher CO_2 solubility than that of water. In addition, the non-aqueous electrolyte can also accurately regulate the amount of water and simplify the mechanism investigation. What is more, ionic liquid can even coordinate with CO_2 molecules and thus greatly lower the energy barrier of the initial CO_2 reduction step [104]. For insistence, Sun et al. reported that N-based Cu(I)/C-doped boron nitride (BN–C) composites could achieve a high FE (80.3%) toward acetic acid with a current density of 13.9 mA cm^{-2} in the 1-ethyl-3-methylimidazolium tetrafluoroborate ([Emim]BF_4)–LiI-water electrolyte [105]. Particularly, the LiI in the ionic liquid electrolyte played a key role in promoting the C–C coupling into acetic acid in the electrocatalytic CO_2 reduction process. Recently, a solid electrolyte has been developed for CO_2 reduction with the advantages of readily separation of the products from the electrolyte, which is a challenge in aqueous and other non-aqueous electrolytes [106,107]. Further development on the design of solid electrolytes for exclusive C_{2+} production may have a great potential.

3.2.3. Electrode (catalyst)

Electrode materials made of electrocatalysts are the main reaction location of CO_2 reduction. Thus, tremendous efforts have been devoted to improving the multicarbon product selectivity by tuning the catalyst composition, morphology, structure, etc. Because Cu-based electrocatalysts are considered to be the most promising one for multicarbon production in CO_2 reduction, we will mainly discuss the strategies toward enhancing C_2 selectivity based on Cu-based materials.

3.2.3.1. Composition

3.2.3.1.1. Cu^+. Oxide-derived copper (OD-Cu) exhibited unprecedented catalytic activity toward electrocatalytic CO_2 reduction, with low onset potentials and excellent C_{2+} product selectivity [108]. Although the activity origin has not been totally understood, the surface-oxidized Cu sites seemed to be a critical factor [109]. Generally, the OD-Cu electrocatalysts were prepared through

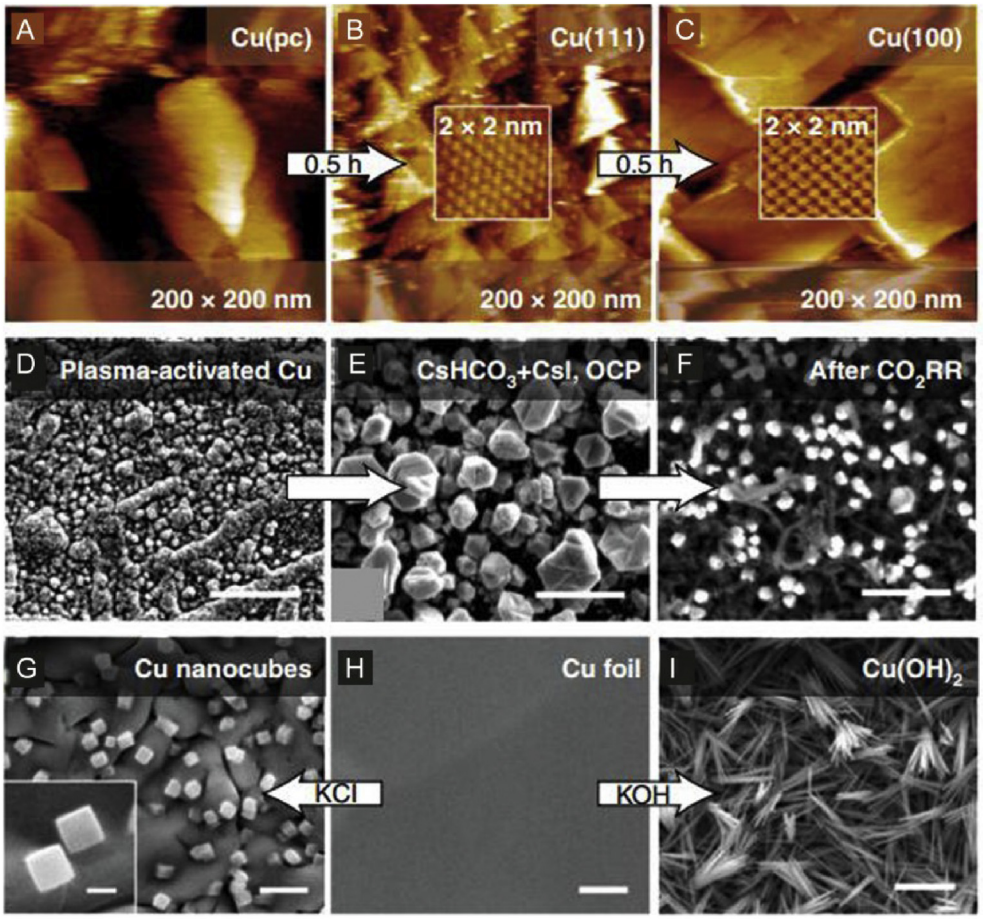

Fig. 16. Effect of electrolyte on catalyst structure. (A–C) EC-STM images of polycrystalline Cu after different reaction times under CRR at −0.90 V (vs. standard hydrogen electrode [SHE]) in 0.1 M KOH [8,93]; (D–F) SEM images of O_2 plasma-oxidized Cu foil (D), and after immersion in $CsHCO_3$+CsI at open circuit potential (E) and after 1 h of CRR at −1.0 V vs. RHE (F), all the scale bars are 5 μm [8,85,94]; (G–I) SEM images of a pristine metallic Cu foil (H, scale bar is 2 μm), and a similar Cu foil after cycling in KCl (G, scale bars is 2 μm [image] and 200 nm [insert]) and in KOH (I; scale bar is 5 μm) [8,96,97]. CRR, CO_2 reduction reaction; SEM, scanning electron microscopy; RHE, reversible hydrogen electrode. Reproduced with permission from Gao et al. [8]. Copyright 2019, Springer Nature.

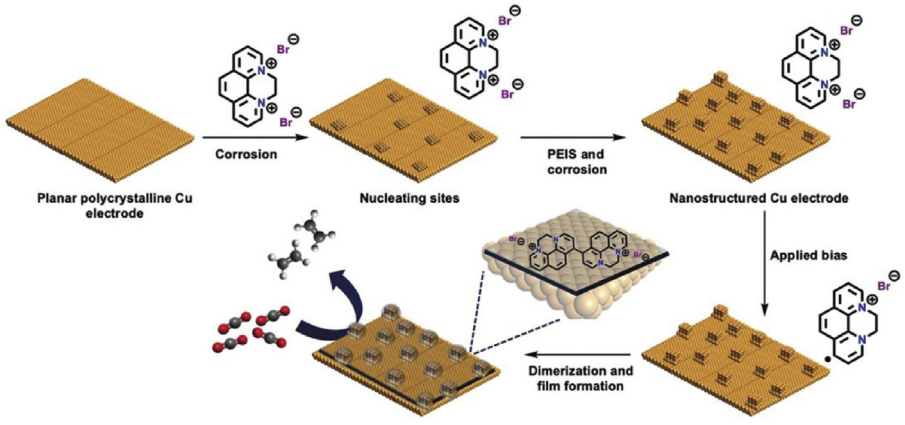

Fig. 17. Proposed work mechanism of **1-Br$_2$** additive on a polycrystalline copper electrode. PEIS, potentiostatic electrochemical impedance spectroscopy. Reproduced with permission from Thevanon et al. [99]. Copyright 2019, John Wiley & Sons, Inc.

purposeful oxidation and subsequent *in situ* electrochemical reduction. The thermodynamic potential for Cu_2O reduction into Cu is −0.36 V (NHE), which is usually more positive than the CO_2 reduction potential windows [20]. Some Cu^+ can retain under the CO_2 reduction conditions [109]. This may be attributed to the sufficiently slow reduction process and the generation of local high pH environment during CRR, which can negatively shift the reduction potential of Cu_2O and thus stabilizing Cu^+ [110]. To study the working mechanism of Cu^+ in CO_2 reduction, Xiao et al. [95] constructed a Cu metal embedded in the oxidized matrix (MEOM)

model with quantum mechanics methods. They found that the separate Cu^+ actually deteriorates the CO_2RR performance. However, the study on the MEOM model showed that the surface Cu^+ and surface Cu^0 could synergistically promote both CO_2 activation and CO dimerization, thereby boosting the activity and C_{2+} selectivity of CO_2RR (Fig. 18A) [95]. The Cu^+ could strongly absorb H_2O molecules via hydrogen bonds and stabilize CO_2 molecule in the initial step. Particularly, the charge of *CO on Cu^+ was +0.11, while the charge of *CO on Cu was totally adverse as −0.31 [95]. Therefore, two *CO molecules on the adjacent Cu^+ and Cu sites will be preferable for C−C bond coupling under the electrostatics interaction, leading to the enhancement of C_2 selectivity. Based on this principle, Jiao et al. [111] reported an atomically designed catalyst with two adjacent copper atoms for CO_2 reduction (Fig. 18B). The two Cu atoms in the pair exhibited +1 and 0 valence states, respectively, where the Cu^+ site adsorbs H_2O and the neighboring Cu^0 site adsorbs CO_2. Zhou et al. [112] reported that the ratio of $Cu^{\delta+}$ to Cu^0 sites could be tuned by boron doping. Thus, the CO adsorption and dimerization on the catalyst surface can be controlled toward high C_2 product selectivity. As a result, an experimentally high C_2 FE of 79 ± 2% and over 40-h stability were achieved on the boron-doped copper catalysts [112]. Besides the Cu oxide, Yin et al. [113] recently reported a copper(I) nitride (Cu_3N) nanocube (NC) with perovskite-type structure. They thought the Cu(I) site in the Cu_3N structure could promote CO−CHO coupling on the (100) facet, favoring the selective formation of C_2H_4 [113]. Experimentally, the 25-nm Cu_3N NCs exhibited high ethylene selectivity (60% of FE) and mass activity (34 A/g) [113].

Although the critical role of Cu^+ in enhancing C_2 product selectivity has been widely reported, some opposite experimental phenomena have also been observed. Mandal et al. [114] investigated the CO_2RR on various Cu_2O catalysts, including Cu_2O nanoneedles and Cu_2O NPs, with selected-ion flow tube mass spectrometry, *in situ* Raman spectroscopy, and computational modeling technologies. They found that the C_2 products were not generated until Cu_2O was being totally reduced into Cu because the reduction of Cu_2O was kinetically and energetically more favorable than the reduction of CO_2. Ren et al. [115] also observed that the *CO vibrations only occur after the disappearance of Cu−O vibrations from Cu_2O from the *in situ* Raman spectroscopy study. In addition, from the *in situ* X-ray absorption spectroscopy study, Eilert et al. [116] also found that no Cu^+ remains on the Cu surface after CRR operation. Our recent work also shows the coexistence of Cu^+ and Cu^0 by the *in situ* electron energy loss spectroscopy and *in situ* x ray absorption spectroscopy when the product is methanol [56].

3.2.3.1.2. Surface oxygen. Besides the Cu^+, Favaro et al. [117] also found that the subsurface oxygen plays a critical catalytic role in enhancing Cu catalyst's C_2 product selectivity by increasing the surface coverage of *CO. However, Lum and Ager [118] doubted the stability of subsurface oxygen under CRR conditions. They synthesized ^{18}O-enriched OD-Cu catalysts and used them to catalyze the CO_2 reduction. Although the high C_2/C_3 product selectivity (ca. 60% FE) of those catalysts, there was only a very small fraction (<1%) of the original ^{18}O content remaining after only ~10 min of CO_2 reduction reaction at −1.0 V vs RHE. The role of Cu^+ in CO_2 reduction is still in debate, whether it is the direct active site or indirectly affects the electronic structure of Cu through promoting the subsurface oxygen formation or neither. Our recent study indicates Cu^+ is not only a direct active site for CO_2 reduction but also promotes the activation of subsurface oxygen in the lattice by the *operando* multimodal imaging and spectroscopy and isotope experiments [56]. Notably, Lum and Ager [118] pointed out that the OD-Cu may be reoxidized rapidly under ambient conditions and thus may influence the accuracy of *ex situ* method−derived conclusion.

3.2.3.1.3. Hybrid. Cu catalyst is one of the few metals that can catalyze CO_2 reduction into both C_1 and C_2 products with acceptable activity and efficiency. However, its selectivity toward multicarbon products limits its application [6]. Alloying Cu with a second metal has shown a great potential in improving the C_2 selectivity because it can break the inherent binding energy scaling relation of most reaction intermediates [119,120]. To study the origin of high CO_2 reduction selectivity in the Cu-based alloy system, Ma et al. [121] developed a series of bimetallic Cu−Pd catalysts, including ordered, disordered, and phase-separated CuPd structures, as well as two additional disordered Cu_3Pd and $CuPd_3$ structures (Fig. 19A). They found that the phase-separated CuPd and Cu_3Pd structures favor the formation of C_2 products with FE > 60%, while the ordered CuPd catalyst facilitates C_1 product generation (FE > 80%) [121]. This suggests that the neighboring Cu atoms in phase-separated structure may play a critical promoting role in the C_2 selectivity through increasing the probability of C_1 intermediates dimerization, while the alternating Cu−Pd arrangement in ordered structure is mainly in charge of C_1 selectivity. However, the mechanism is still unclear and needs further investigation. The surface valence band spectra study further manifested that the geometric effects seem to be a decisive factor for C_2 selectivity. Ren et al. [122] developed a tandem catalyst model in the Cu-based alloy catalyst system. In the Cu−Zn alloy catalyst, Zn could continuously reduce CO_2 into CO, and subsequently, those generated CO could diffuse into the neighboring Cu sites to couple with the C_1 intermediates on the Cu site (Fig. 19B and C). As a result, the maximized ethanol production was achieved on Cu_4Zn catalyst with an FE of 29.1% under -8.2 mA cm^{-2} [122]. Furthermore, some other CO generation metals such as Ni, Au, Ag, etc. have been applied in a Cu-based alloy catalyst. These alloy systems can not only improve the C_2 selectivity by the synergistic effect of the bimetal sites but also overcome the low solubility of CO through inputting CO_2 as reacting gas. Subsequently, Lee et al. [123] studied the alloy synergistic effect in a phase-separated Ag−Cu_2O catalyst. They found that incorporation of Ag into Cu_2O could boost the ethanol selectivity with a 3-times increase of FE, which should be assigned to the CO population increase arising from the CO generation ability of the Ag site [123]. Moreover, in comparison with the phase-separated Ag−Cu_2O catalyst, the phase-blended one exhibited higher ethanol selectivity even with lower surface Ag content. This result indicated that the distribution and distance between Cu and Ag atoms may influence the transfer efficiency of CO from Ag to Cu sites and thus affect the product selectivity.

Besides the simple Cu-based alloy catalyst, Lum and Ager [124] also demonstrated the synergistic effect of the bimetal sites on well-fabricated micropatterned electrodes. A CO-generating catalyst (Au or Ag) was positioned around the Cu catalyst. In the Cu−Au bimetallic device, the local CO concentration was modulated by the interdigitated or independent lines of Au and Cu. They conducted the diffusional simulations and found that the saturation concentration of CO can be exceeded locally in the interdigitated system [124]. Based on this principle, Morales-Guio et al. [125] loaded the Au NPs on polycrystalline copper foils, which achieved an over 100 times enhancement of C_2 selectivity in electrocatalytic CO_2 reduction process compared with the pure Cu foil. The Au NPs provide a high CO concentration around Cu, and then CO was further reduced into C_2 products on Cu sites. In addition, Lum and Ager [124] continued their study in a Cu−Ag bimetallic system. They fabricated Cu dots/lines patterned directly onto the Ag substrate with a precisely controllable distance between Cu and Ag. By tuning the relative areas of Cu and Ag, the distribution of C_2 product can be

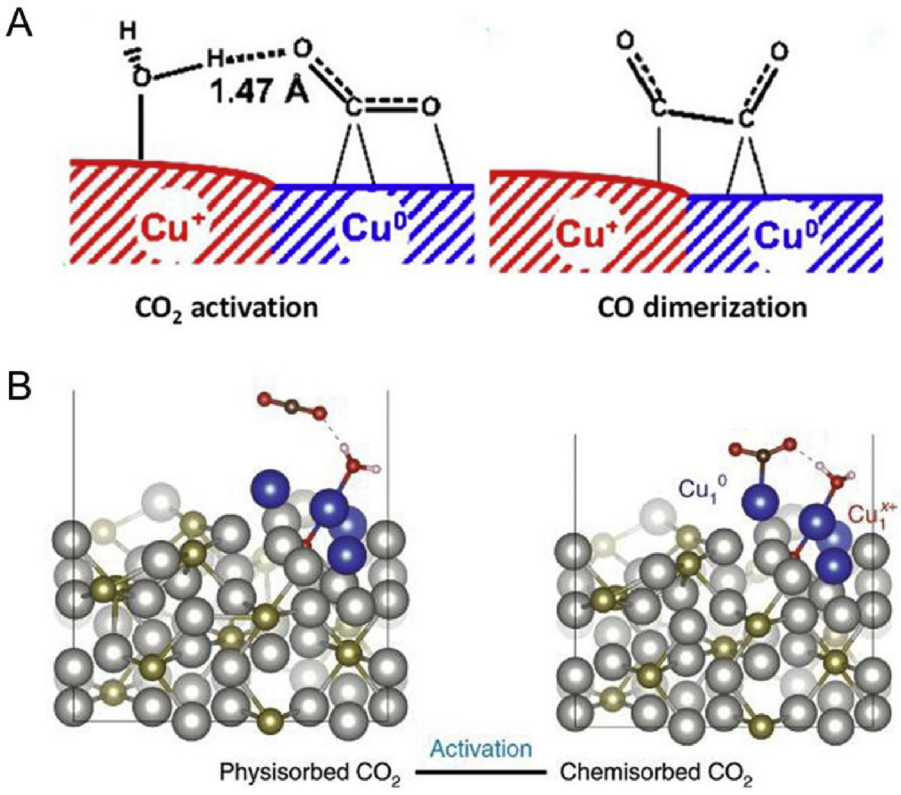

Fig. 18. (A) Proposed synergistic mechanism of Cu and Cu^+ for CO_2 activation (left) and CO dimerization (right) processes. Reproduced with permission from Xiao et al. [95]. Copyright 2017, National Academy of Sciences. (B) Scheme of physisorbed CO_2 and chemisorbed CO_2 configurations on Cu atom-pair catalysts. Reproduced with permission from Jiao et al. [111]. Copyright 2019, Springer Nature.

continuously adjusted. The proportion of C_2H_4 can be varied from 0.53 to 0.24, and the fraction of oxygenates from 0.33 to 0.67, while the CH_4 remains unchanged [124]. Apart from the bimetal sites, Pang et al. [126] also found the synergistic effect of mixed crystal facets. They developed a Cu catalyst composed of the fragmented structures of Cu(200) and Cu(111) facets, which were responsible for C_1 and C_2 intermediates, respectively [126]. Thus, the highly mixed facets can bring C_1 and C_2 binding sites together and thus accelerate the coupling of these intermediates into n-propanol, resulting in a 20% FE of n-propanol.

3.2.3.2. Morphology

3.2.3.2.1. Facet. The morphology of nanocatalysts usually plays a significant role in the electrocatalytic CO_2RR processes. In general, different morphology (shape) is surrounded by different facets. To clarify the relationship between facets and CO_2RR selectivity, Hori et al. [127] studied the performance of CO_2 reduction on a series of copper single-crystal electrodes. They found that the electrocatalytic CRR product selectivity strongly depends on the facets, Cu (100) selectively favoring the formation of ethane, Cu(110) favoring C_2 products, while Cu(111) favoring C_1 products. To further distinguish the origin of ethane selectivity on Cu (100) facet, Schouten et al. [128] systematically studied the CO reduction on Cu (322), with the [5(111) × (100)] orientation, and Cu(911), with the [5(100) × (111)] orientation. They observed that ethylene can only selectively be formed on Cu(911), suggesting the active sits for ethylene was the (100) terraces rather than the (100) steps [128]. Wang et al. [129] carried out the comparative study of electrocatalytic CO_2 reduction on Cu nanocubes and nanospheres. The Cu nanocubes with preferentially exposed (100) facets exhibited apparent enhancement in ethylene activity and selectivity compared with the Cu nanospheres with majority (111) facets. Specifically, the Cu nanocubes attained a high ethylene FE of 60% and a partial current density of 144 mA cm^{-2} in a gas diffusion electrode system with flowing alkaline catholyte. Loiudice et al. [130] carefully investigated the electrocatalytic CO_2 reduction performance of a series of Cu nanocubes with different sizes and shapes, which were produced from the same colloidal approach. They found that the C_2 product selectivity was directly related to the size of Cu nanocubes. Among 24-nm, 44-nm, and 63-nm nanocubes tested, the Cu nanocubes with the size of 44 nm displayed the highest C_2 product selectivity with 41% FE of ethylene [130]. This indicates that the ratio of edge sites and plane sites of (100) facet may play a critical role in the ethylene selectivity. Jiang et al. [98] reported a metal-ion battery cycling method to tune the facet exposure on Cu foil and investigated the electrocatalytic CO_2 performance. Combined with the DFT calculation, they found that the stepped (211) facets can also promote C_{2+} product formation as (100) facet. Grosse et al. [131] studied the dynamic changes in the structure, chemical state, and catalytic selectivity of ligand-free Cu nanocubes during the electrocatalytic CO_2 reduction process, by *operando* electrochemical atomic force microscopy and X ray absorption spectroscopy. They found that the Cu (100) facets gradually disappeared with the loss of Cu and reduction of CuO_x species under reaction conditions, which leads to the suppression of multicarbon product selectivity. Those results raised the stability issue of facet-selected nanocatalysts in electrocatalysis. The well-defined facets may degrade and cause the deactivation of selectivity under the electrocatalytic CO_2 reduction process. In addition, Duan et al. [132] found the amorphous Cu NPs possess excellent ethanol selectivity with 22% FE at −1.4 V, while the crystalline Cu NPs could not produce any C_2 product during the electrocatalytic

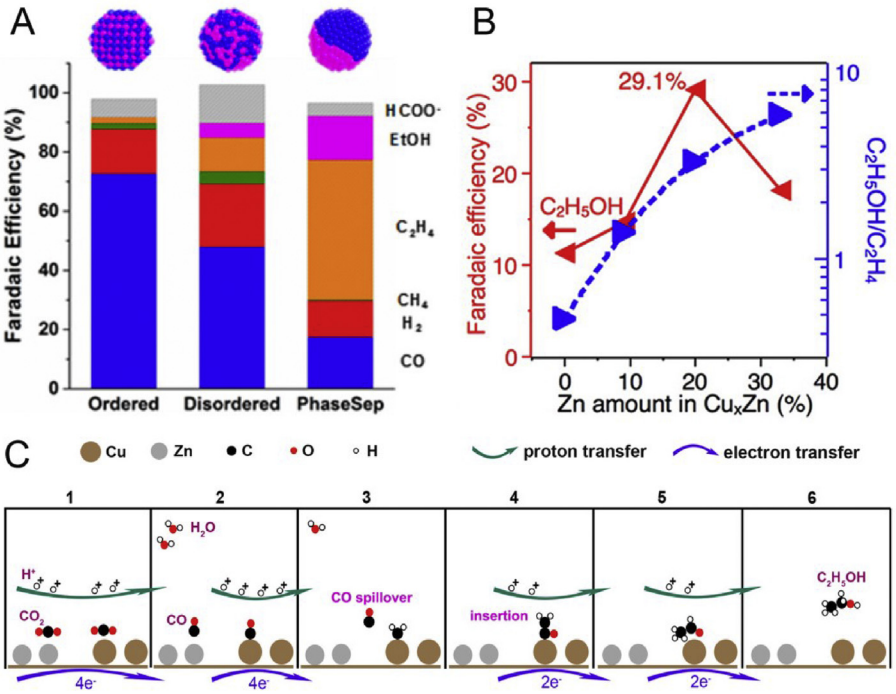

Fig. 19. (A) Scheme of ordered, disordered, and phase-separated CuPd nanoalloy structure and corresponding CRR product selectivity. Reproduced with permission from Ma et al. [121]. Copyright 2017, American Chemical Society. (B) The change of FE of ethanol and FE ratio of ethanol with Zn amount in the Cu–Zn alloy catalyst; (C) proposed mechanism of ethanol formation from the electrocatalytic CRR process over Cu–Zn alloy catalyst; water molecules are assumed to be the proton carriers. FE, Faradaic efficiency; CRR, CO_2 reduction reaction. Reproduced with permission from Ren et al. [122]. Copyright 2016, American Chemical Society.

CO_2 reduction test. This work suggested a possible avenue for C_2 selectivity based on amorphous metal catalysts. But the mechanism is still unclear.

3.2.3.2.2. Mass transport structure. As discussed on the influence of electrolyte, the bulk pH greatly affects the CO_2 reduction pathway and the product selectivity. The different product selectivity can be resulted from the local pH around the catalyst surface, which can be tuned by either bulk pH or buffer solution. Ma et al. [133] found that the morphology of Cu NWs also had a great influence on the surface local pH and resulted in different product selectivity (Fig. 20A). They controllably synthesized a series of Cu NW array catalyst with different lengths and densities. The electrocatalytic test showed that the CO_2 reduction product selectivity for multicarbon hydrocarbons under a fixed potential could be adjusted by tuning the length and density of the Cu NW [133]. The FE for C_2H_4 production gradually increased with the Cu NW arrays being longer and denser. Notably, the catalyst with 8.1-mm-length Cu NW displayed the highest FE for C_2H_4 (17.4%). As shown in Fig. 20B, the increase of NW length and density may retard the diffusion of generated OH^- out of Cu NW arrays and the diffusion of HCO_3^- into Cu NW array. Such a limited diffusion process can cause a slow neutralization reaction of OH- generated near the catalyst surface, resulting in a local high OH- concentration around the catalyst surface, namely a high local pH. To further understand the relationship between catalyst morphology and local pH, Raciti et al. [134] developed a mass transport model based on Cu NW catalyst for electrocatalytic CO_2 reduction. By solving the mass balance partial differential equations (PDEs), the local concentrations of different species and the spatial distribution of electrocatalytic reactions along the NWs were calculated. The mass transport effects toward electrocatalytic CO_2 reduction were directly linked to the surface local pH. The calculation results showed that the local pH is an indicator of the potential-dependent concentrations of reaction species. Thus, the local pH affected the mass transport and reaction kinetics. The local pH range of 9–10 was found to be an optimal range for the Cu NW catalysts [134]. A high local pH can balance the beneficial aspects of improving C_2 product selectivity with the detrimental aspect of the shifted acid-base–limited CO_2 diffusion issue. Lately, Raciti et al. [135] also systematically investigated the mass transfer effects on electrocatalytic CO_2 reduction under practically relevant high-flux conditions based on highly dense Cu NWs. They found that the limited mass transfer of CO_2 placed an upper limit on the electrocatalytic CO_2 reduction activity under large current densities [135].

3.2.3.2.3. Pore structure. Dutta et al. [136] investigated the influence of porous structure on electrocatalytic CO_2 reduction using a number of oxide-derived mesoporous Cu foams (Fig. 21A). They found the C_2 selectivity was strongly dependent on the surface pore size of the Cu catalysts. A maximal C_2 selectivity with 55% FE was achieved on the mesoporous Cu foams with pore diameters between 50 and 100 μm (Fig. 21B) [136]. Besides the surface oxidation state, the gaseous trapping ability of the porous structure in the Cu foams was a vital factor for the high C_2 selectivity. Trapping of gaseous intermediates, such as CO and C_2H_4, would cause a longer residence time inside the pores. Thus, it increases the probability of gaseous intermediate readsorption and further promotes reduction on the Cu catalyst for C_2 selectivity. As shown in Fig. 21C, the trapping efficiency of gaseous intermediates was found to deeply rely on the Cu foam catalyst's morphology [136].

3.2.3.3. Structure

3.2.3.3.1. Grain boundaries. Compared with polycrystal Cu, the OD-Cu possesses a much higher density of grain boundaries (GBs). Thus, a GB has been considered as the possible active site of OD-Cu catalysts, besides the Cu^+ and subsurface oxygen [137]. Verdaguer-Casadevall et al. [138] found that the high CO reduction activity could be achieved on OD-Cu, attributed to the stronger CO binding ability of GB sites in OD-Cu catalyst than low-index and stepped

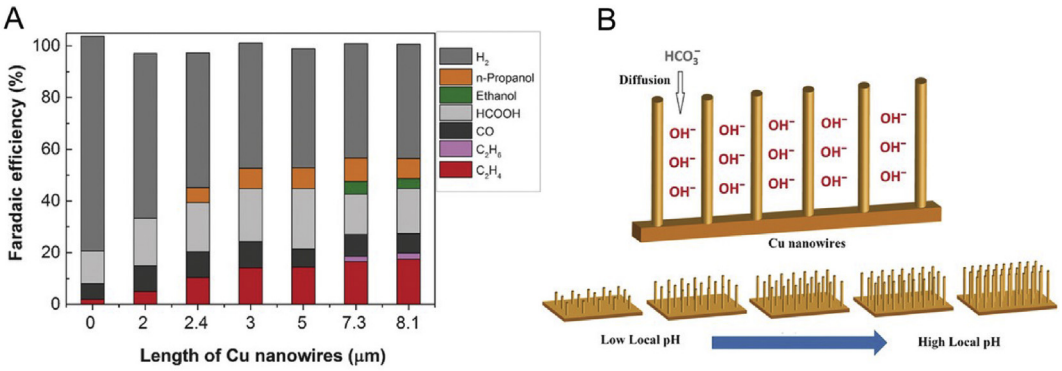

Fig. 20. (A) FE for different products on Cu nanowire arrays with different lengths at −1.1 V vs. RHE in CO_2-saturated 0.1 M $KHCO_3$; (B) scheme of the diffusion of electrolytes into Cu nanowire arrays. FE, Faradaic efficiency; RHE, reversible hydrogen electrode. Reproduced with permission from Ma et al. [133]. Copyright 2016, John Wiley & Sons, Inc.

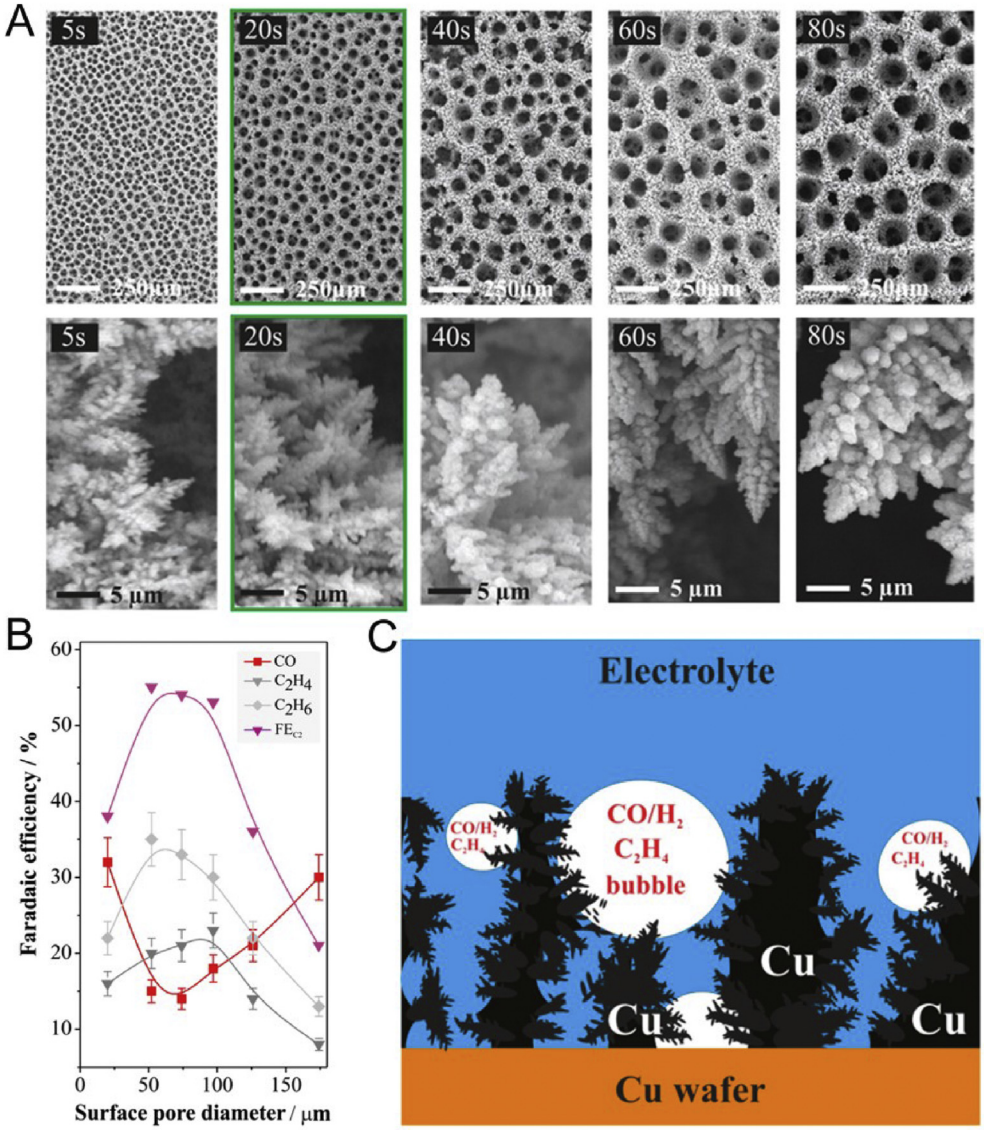

Fig. 21. (A) SEM images of Cu foams prepared with different deposition time; (B) scheme of trapped different gaseous products and intermediates of electrocatalytic CRR inside the Cu foam catalyst; (C) the relationship between FE of different products and pore size of the Cu foam catalyst. FE, Faradaic efficiency; CRR, CO_2 reduction reaction; SEM, scanning electron microscopy. Reproduced with permission from Dutta et al. [136]. Copyright 2016, American Chemical Society.

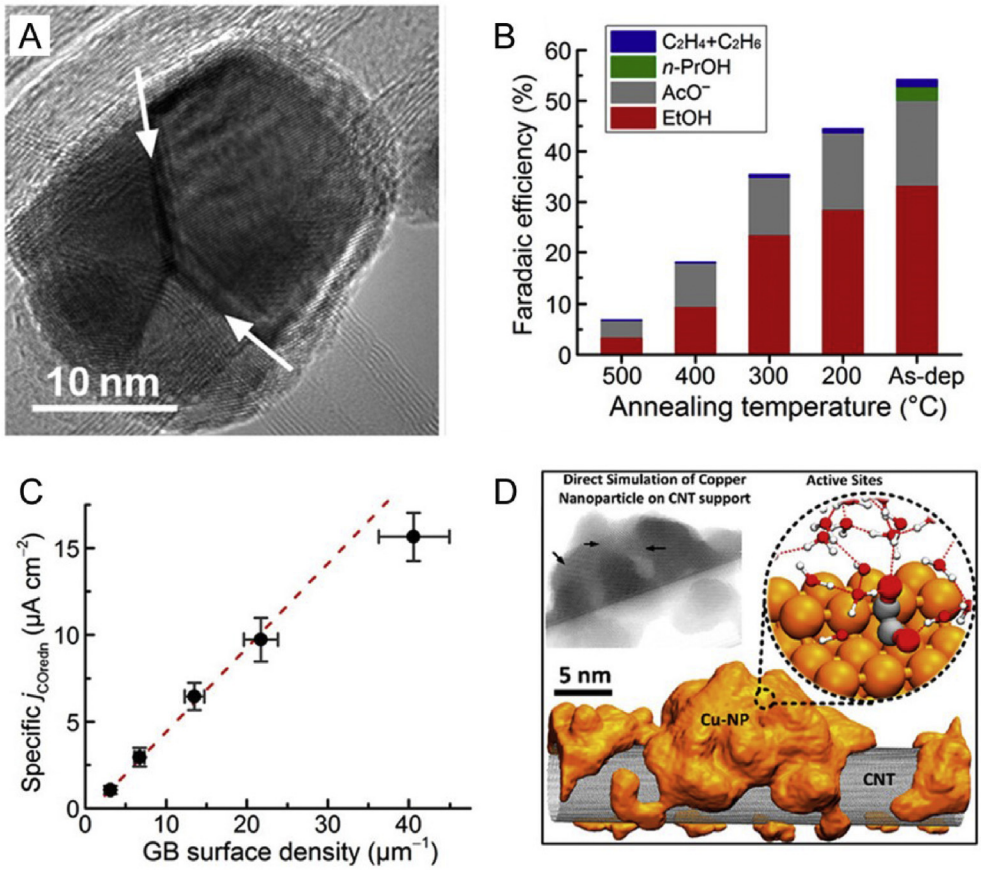

Fig. 22. (A) TEM image of Cu NPs on CNTs; the grain boundaries are indicated by the arrows. (B) FE of different products from electrocatalytic CO reduction over different samples. (C) The relationship between specific current density of CO reduction and the GB surface density in Cu NPs catalysts. Reproduced with permission from Feng et al. [139]. Copyright 2016, American Chemical Society. (D) Atomic structure and *CO–COH adsorption (inset) of the computationally synthesized Cu NPs on CNTs. CNTs, carbon nanotubes; TEM, transmission electron microscopy; FE, Faradaic efficiency; NP, nanoparticle; GB, grain boundary. Reproduced with permission from Cheng et al. [140]. Copyright 2017, American Chemical Society.

Cu facets. This strong CO binding ability of GB may promote the C_2 selectivity of electrocatalytic CO_2 reduction on the OD-Cu catalyst. Feng et al. [139] established a correlation between the densities of GBs and the electrocatalytic activity of CO reduction toward C_2H_5OH or CH_3COO^- on Cu NP catalyst. They prepared carbon nanotubes–supported Cu NPs with different average GB densities which were measured by transmission electron microscopy (TEM) (Fig. 22A) [139]. The density and length of GBs in the Cu NPs catalyst were controlled to tune electrocatalytic activities (Fig. 22B) [139]. A linear relationship was found between the surface GB densities of OD-Cu and the CO reduction activity (Fig. 22C) [139]. Correspondingly, Cheng et al. [140] found that not all *CO-binding sites were active for C_2 product based on a multiscale simulation study. Instead, only the relative sites with the under-coordinated neighbor square site could promote C–C coupling (Fig. 22D) [140].

3.2.3.3.2. Surface modification. Ahn et al. [141] proposed a polyamide modification method to improve the multicarbon product selectivity of Cu catalyst. The modification of poly(acrylamide) on electrodeposited copper foam caused a substantial enhancement of ethylene selectivity, with FE increased from 13% to 26% [141]. The mechanism of poly(acrylamide) was revealed by DFT calculations. It can be ascribed to three aspects: (i) poly(acrylamide) enhanced the dimerization of CO through donating charge to the Cu surface; (ii) poly(acrylamide) stabilized the CO dimer through the hydrogen bond interactions of $-NH_2$ group with CO; (iii) poly(acrylamide) increased the surface coverage of CO molecules by facilitating the adsorption of CO molecules around the polymer [141]. Han et al. [142] reported a simple but effective method to improve the multicarbon product selectivity of polycrystalline Cu electrode in 0.1 M $KHCO_3$ with N-substituted pyridinium additives (Fig. 23A). The N-substituted pyridinium additives were deposited on the surface of the Cu electrode upon electroreduction. Therefore, it modified the local environment. As a result, the selectivity of multicarbon products reached 70–80% with the additives. Nevertheless, the ethylene selectivity (~40% FE) and partial current density (0.5 mA cm^{-2}) were relatively low for practical applications [142]. Following this study, Li et al. [143] assumed that the enhancement of the CO_2RR selectivity may be derived from the interaction of the N-arylpyridinium film and the reaction intermediates. To verify this hypothesis, they prepared 11 *N*-arylpyridinium salts and studied their role in the electrocatalytic CO_2 reduction on Cu catalyst. They found a volcano-shaped relationship between the FE and Bader charge [143]. Particularly, the tetrahydro-bipyridine with moderate electron-donating ability exhibited the highest ethylene selectivity [143]. Further study showed that the tetrahydro-bipyridine film could stabilize *CO intermediate by transferring an electron to *CO through H_2O mediator. Therefore, the dimerization of CO was promoted and the ethylene selectivity was enhanced. However, experimental evidence has showed that the tetrahydro-bipyridine could neither modulate the structure and electronic environment of Cu nor

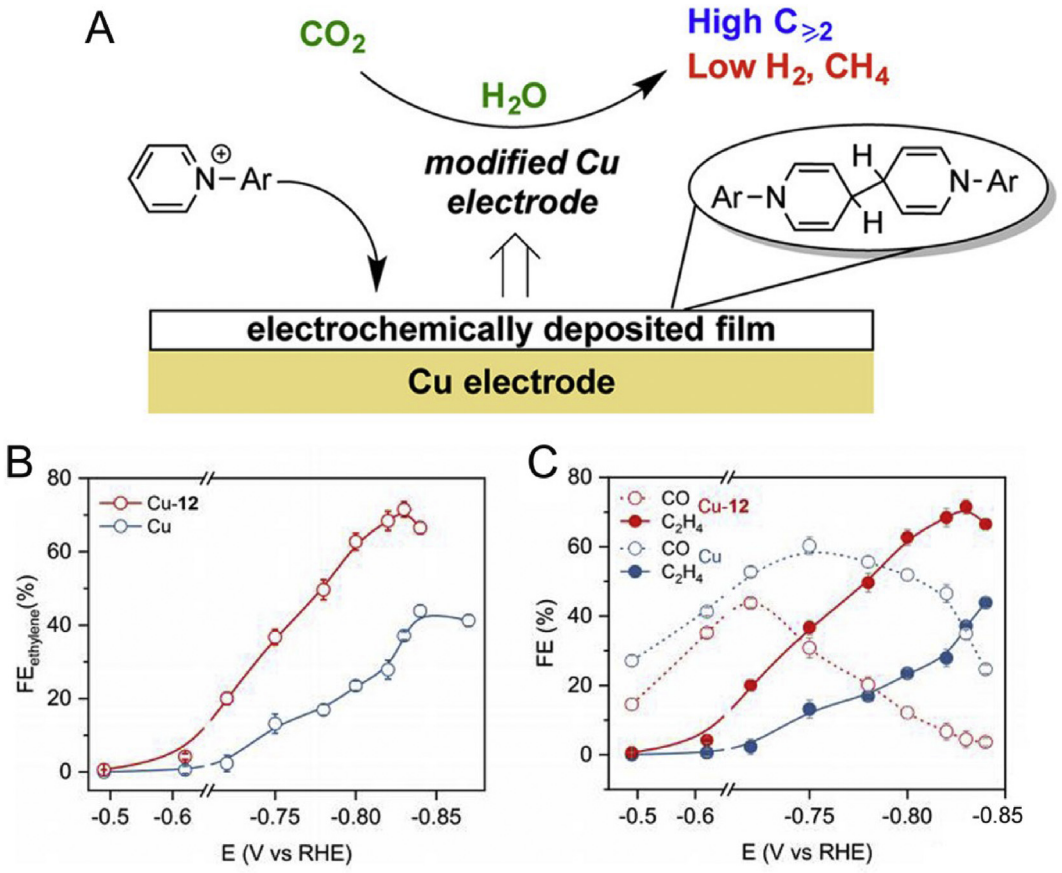

Fig. 23. (A) Scheme of electrocatalytic CRR process on poly(acrylamide)−modified electrodeposited copper foam; Reproduced with permission from Han et al. [142]. Copyright 2017, American Chemical Society. (B) FE of ethylene on Cu and Cu-12 in CO_2-saturated 1 M $KHCO_3$; (C) FE of CO and ethylene on Cu and Cu-12 under the applied potential range of −0.47 to −0.84 V. CRR, CO_2 reduction reaction; FE, Faradaic efficiency; RHE, reversible hydrogen electrode. Reproduced with permission from Li et al. [143]. Copyright 2019, Springer Nature.

mediate the electron and proton transfer steps [143]. Considering the *CO binding may be influenced by the nitrogen atom of the N-aryl−substituted pyridine ring, they synthesized an N,N'-(1,4-phenylene)bispyridinium salt (**12**) with optimal electron-donating properties and more nitrogen sites to stabilize more *CO on Cu surface [143]. As a result, a high ethylene selectivity of 72% FE under a partial current density of 230 mA cm^{-2} was achieved in neutral medium (Fig. 23B and C) [143]. Moreover, the excellent performance could be maintained for 190 h in a membrane electrode assembly−based catalytic system with a full-cell energy efficiency of 20% [143].

4. Summary and outlook

Significant breakthroughs have been made in the research of CRR to C_2 products by photocatalysis and electrocatalysis methods. However, current techniques are still far from being implemented as large-scale production technologies because of the relatively low C_2 product selectivity and the activity and stability of the catalysts. Particularly, most of the current studies on multicarbon products usually report on a mixture of multicarbon products rather than a relatively pure multicarbon product, which is distinct from the nature photosynthesis. As a result, a high cost is expected for separating the products. The catalytic activity is often ignored when the selectivity of multicarbon products is discussed. Besides, the long-term stability of the catalyst is very important and should be considered. To facilitate the development of CRR technology from the laboratory to market, future research should be focused on the following critical aspects.

(i) **Catalyst.** Most studies of C_2 products are intensively concentrated on Cu-based catalyst because of the exclusive C−C coupling ability of Cu. However, some very recent research studies reported on producing of multicarbon products on non-Cu catalysts, such as MoS_2, heteroelement-doped carbon, Ag, Pd, etc. [144−150] The emergence of those multicarbon production using non-Cu catalysts enriches the categories of alternative catalysts. More importantly, the structure-performance relationship on those non-Cu catalysts can provide alternative methods for multicarbon species production. For example, Song et al. [151] found that the selective formation of ethanol could be promoted by creating medium micropores in nitrogen-doped ordered mesoporous carbon. Zhuang et al. [148] found the metallic Pd with boron doping can produce C_3 product (dimethyl carbonate) from electrocatalytic oxidative carbonylation of CO and methanol, by tuning the binding strength of intermediates. Those interesting findings on non-Cu catalysts may indicate different mechanisms from that on Cu-based catalysts, which should be used to guide more creative catalyst developments.

(ii) **Mechanism of reaction processes.** Mechanisms of the reaction process can reveal the reaction pathways, which are of crucial importance for catalyst design and reaction

condition optimization. The research on reaction mechanisms is usually performed by conducting the advanced *operando* measurements, such as *operando* selected-ion flow tube mass spectrometry (SIFT-MS), *in-situ* Fourier-transform infrared spectroscopy (FTIR), *in-situ* Raman spectra, *in situ* TEM, *in situ* X-ray absorption fine structure (XAFS), etc. [56,114,152]. Although great advances have been achieved on identifying the mechanisms by those *operando* studies, the complete CO_2 reduction mechanism is still unclear because of the limitations of each individual *in situ* technique. Moreover, most of the *operando* measurements are carried out at different length scales. For example, the *in situ* FTIR probes just a thin electrolyte layer with limited mass transportability, which is strikingly different from the measurement of bulk electrolyte properties at the larger scale. *In situ* X-ray absorption spectroscopy (XAS) and X-ray diffraction (XRD) only probe the ensemble properties, which are difficult to investigate the heterogeneous mechanisms of the catalysts. Therefore, the acquired results from a single *in situ* technique may be unsuitable to reflect the real mechanism. Thus, developing multiscale *operando* techniques under the realistic reaction conditions is particularly important for recognizing the most authentic and comprehensive reaction mechanism [56].

In addition, theoretical calculations can provide valuable support to the *operando* measurements on revealing the mechanisms of reaction processes. However, the vast majority of current theoretical calculations only considered the thermodynamic energy barrier on the simplified structure model of the catalyst surface. This treatment ignored many other aspects, such as kinetic barrier, solvent effects, applied potentials, catalyst inner structure, etc. [20]. Such unilateral calculations may result in inaccurate conclusions. Therefore, similar to the *operando* study, a theoretical modeling study is also highly recommended to consider multidimensional factors of the realistic reaction conditions and true properties of catalyst structures. Also, additional calculation parameters may greatly increase the computational complexity and computation time. Thus, the development of suitable simulation methods is also essential to understand the mechanism.

(iii) **Reactor design.** The configuration of the reactor is often overlooked in catalysis studies. Usually, an H-type cell with membrane-separating two compartments is used to conduct the electrocatalytic CO_2 reduction. Although it is convenient to use H-type cells in the small-scale studies, the cells are not suitable for the large-scale industrial application because of the mass transport limitations, high internal resistance (IR) losses, and low current densities [82]. To fulfill the requirements of industrial application, continuous-flow cells have been developed for electrocatalytic CO_2 reduction. Moreover, the flow cells can be further categorized in membrane reactors and membrane-less microfluidic reactors with liquid or gaseous input reactants. In other words, the reactor configuration and reaction parameter may greatly affect the product distribution and yield. Thus, the reactor and reaction parameters should be carefully designed.

(iv) **Techno-economic analysis.** Catalytic conversion of CO_2 into multicarbon chemicals can not only remove excess carbon dioxide from the atmosphere but also create value-added products. The improvement of CO_2 reduction selectivity also provides a higher yield and a larger economic value of those products compared to the C_1 products. Techno-economic analysis can help approximately quantify he economic viability of the realistic industrial production of certain target molecules. However, the actual economic benefits may be very difficult to assess due to the complexes in evaluating the costs of CO_2, electricity, light, separation of products, capital and maintenance, operation, and product selectivity. Moreover, to better compare the economic values of catalysts and to design products with a more added value, a valid techno-economic analysis should consider all aspects of the CO_2 reduction reactions, especially the catalyst cost, activity, selectivity, and stability.

Declaration of competing interest

The authors declare that they have no known competing financial interests or personal relationships that could have appeared to influence the work reported in this article.

Acknowledgments

Y.A.W. thanks the support from the Natural Sciences and Engineering Research Council (NSERC), Canada.

References

[1] L. Zhang, Z.J. Zhao, J.L. Gong, Angew. Chem. Int. Ed. 56 (2017) 11326–11353.
[2] M.B. Ross, P. De Luna, Y.F. Li, C.T. Dinh, D. Kim, P. Yang, E.H. Sargent, Nat. Catal. 2 (2019) 648–658.
[3] V. Smil, Energy Transitions: History, Requirements, Prospects, ABC-CLIO2010.
[4] J.H. Wu, Y. Huang, W. Ye, Y.G. Li, Adv. Sci. 4 (2017) 1700194.
[5] C. Hepburn, E. Adlen, J. Beddington, E.A. Carter, S. Fuss, N. Mac Dowell, J.C. Minx, P. Smith, C.K. Williams, Nature 575 (2019) 87–97.
[6] S. Nitopi, E. Bertheussen, S.B. Scott, X.Y. Liu, A.K. Engstfeld, S. Horch, B. Seger, I.E.L. Stephens, K. Chan, C. Hahn, J.K. Norskov, T.F. Jaramillo, I. Chorkendorff, Chem. Rev. 119 (2019) 7610–7672.
[7] O.S. Bushuyev, P. De Luna, C.T. Dinh, L. Tao, G. Saur, J. van de Lagemaat, S.O. Kelley, E.H. Sargent, Joule 2 (2018) 825–832.
[8] D.F. Gao, R.M. Aran-Ais, H.S. Jeon, B.R. Cuenya, Nat. Catal. 2 (2019) 198–210.
[9] X. Li, J.G. Yu, M. Jaroniec, X.B. Chen, Chem. Rev. 119 (2019) 3962–4179.
[10] J. Fu, K. Jiang, X. Qiu, J. Yu, M. Liu, Mater. Today (2019), https://doi.org/10.1016/j.mattod.2019.06.009.
[11] J.L. Qiao, Y.Y. Liu, F. Hong, J.J. Zhang, Chem. Soc. Rev. 43 (2014) 631–675.
[12] S. Matavos-Aramyan, S. Soukhakian, M.H. Jazebizadeh, M. Moussavi, M.R. Hojjati, Appl. Mater. Today (2019) 100499.
[13] N. Armaroli, V. Balzani, Angew. Chem. Int. Ed. 46 (2007) 52–66.
[14] J.J. Concepcion, R.L. House, J.M. Papanikolas, T.J. Meyer, Proc. Natl. Acad. Sci. U. S. A. 109 (2012) 15560–15564.
[15] J. Barber, Chem. Soc. Rev. 38 (2009) 185–196.
[16] S.N. Habisreutinger, L. Schmidt-Mende, J.K. Stolarczyk, Angew. Chem. Int. Ed. 52 (2013) 7372–7408.
[17] X. Chen, S.S. Mao, Chem. Rev. 107 (2007) 2891–2959.
[18] X.X. Chang, T. Wang, J.L. Gong, Energy Environ. Sci. 9 (2016) 2177–2196.
[19] A. Vasileff, C.C. Xu, Y. Jiao, Y. Zheng, S.Z. Qiao, Chem 4 (2018) 1809–1831.
[20] Y. Zheng, A. Vasileff, X.L. Zhou, Y. Jiao, M. Jaroniec, S.Z. Qiao, J. Am. Chem. Soc. 141 (2019) 7646–7659.
[21] W.J. Zhang, Y. Hu, L.B. Ma, G.Y. Zhu, Y.R. Wang, X.L. Xue, R.P. Chen, S.Y. Yang, Z. Jin, Adv. Sci. 5 (2018) 1700275.
[22] J. Qiao, Y. Liu, F. Hong, J. Zhang, Chem. Soc. Rev. 43 (2014) 631–675.
[23] F. Calle-Vallejo, M.T.M. Koper, Angew. Chem. Int. Ed. 52 (2013) 7282–7285.
[24] A.D. Handoko, K.W. Chan, B.S. Yeo, ACS Cent. Sci. 2 (2017) 2103–2109.
[25] M. Jouny, W. Luc, F. Jiao, Nat. Catal. 1 (2018) 748–755.
[26] K.D. Yang, C.W. Lee, K. Jin, S.W. Im, K.T. Nam, J. Phys. Chem. Lett. 8 (2017) 538–545.
[27] Q. Fan, M. Zhang, M. Jia, S. Liu, J. Qiu, Z. Sun, Mater. Today Energy 10 (2018) 280–301.
[28] I. Ledezma-Yanez, E.P. Gallent, M.T.M. Koper, F. Calle-Vallejo, Catal. Today 262 (2016) 90–94.
[29] Y. Hori, R. Takahashi, Y. Yoshinami, A. Murata, J. Phys. Chem. B 101 (1997) 7075–7081.
[30] E.L. Clark, A.T. Bell, J. Am. Chem. Soc. 140 (2018) 7012–7020.
[31] T. Billo, F.Y. Fu, P. Raghunath, I. Shown, W.F. Chen, H.T. Lien, T.H. Shen, J.F. Lee, T.S. Chan, K.Y. Huang, C.I. Wu, M.C. Lin, J.S. Hwang, C.H. Lee, L.C. Chen, K.H. Chen, Small 14 (2018) 1702928.
[32] C.W. Lee, R.A. Kourounioti, J.C.S. Wu, E. Murchie, M. Maroto-Valer, O.E. Jensen, C.W. Huang, A. Ruban, J. CO_2 Util. 5 (2014) 33–40.
[33] T. Phongamwong, M. Chareonpanich, J. Limtrakul, Appl. Catal., B 168 (2015) 114–124.
[34] T. Wu, C. Zhu, D. Han, Z. Kang, L. Niu, Nanoscale 11 (2019) 22980–22988.
[35] C.H. An, S.N. Peng, Y.G. Sun, Adv. Mater. 22 (2010) 2570–2574.

[36] P. Wang, B.B. Huang, X.Y. Qin, X.Y. Zhang, Y. Dai, J.Y. Wei, M.H. Whangbo, Angew. Chem. Int. Ed. 47 (2008) 7931–7933.
[37] L. Han, P. Wang, C.Z. Zhu, Y.M. Zhai, S.J. Dong, Nanoscale 3 (2011) 2931–2935.
[38] Y.A. Wu, L. Li, Z. Li, A. Kinaci, M.K.Y. Chan, Y. Sun, J.R. Guest, I. McNulty, T. Rajh, Y. Liu, ACS Nano 10 (2016) 3738–3746.
[39] B. Cai, J. Wang, D.X. Han, S.Y. Gan, Q.X. Zhang, Z.J. Wu, L. Niu, Nanoscale 5 (2013) 10989–10995.
[40] B. Cai, J. Wang, S.Y. Gan, D.X. Han, Z.J. Wu, L. Niu, J. Mater. Chem. A 2 (2014) 5280–5286.
[41] T.V. Nguyen, J.C.S. Wu, Appl. Catal. A: Gen. 335 (2008) 112–120.
[42] T.V. Nguyen, J.C.S. Wu, C.H. Chiou, Catal. Commun. 9 (2008) 2073–2076.
[43] S.J. Yu, A.J. Wilson, G. Kumari, X.Q. Zhang, P.K. Jain, ACS Cent. Sci. 2 (2017) 2058–2070.
[44] S.J. Yu, A.J. Wilson, J. Heo, P.K. Jain, Nano Lett. 18 (2018) 2189–2194.
[45] W.G. Tu, Y. Zhou, H.J. Li, P. Li, Z.G. Zou, Nanoscale 7 (2015) 14232–14236.
[46] D.R. Dreyer, S. Park, C.W. Bielawski, R.S. Ruoff, Chem. Soc. Rev. 39 (2010) 228–240.
[47] K.P. Loh, Q.L. Bao, G. Eda, M. Chhowalla, Nat. Chem. 2 (2010) 1015–1024.
[48] M.M. Liu, R.Z. Zhang, W. Chen, Chem. Rev. 114 (2014) 5117–5160.
[49] A. Mathkar, D. Tozier, P. Cox, P.J. Ong, C. Galande, K. Balakrishnan, A.L.M. Reddy, P.M. Ajayan, J. Phys. Chem. Lett. 3 (2012) 986–991.
[50] C. Gomez-Navarro, R.T. Weitz, A.M. Bittner, M. Scolari, A. Mews, M. Burghard, K. Kern, Nano Lett. 7 (2007) 3499–3503.
[51] H.C. Hsu, I. Shown, H.Y. Wei, Y.C. Chang, H.Y. Du, Y.G. Lin, C.A. Tseng, C.H. Wang, L.C. Chen, Y.C. Lin, K.H. Chen, Nanoscale 5 (2013) 262–268.
[52] I. Shown, H.C. Hsu, Y.C. Chang, C.H. Lin, P.K. Roy, A. Ganguly, C.H. Wang, J.K. Chang, C.I. Wu, L.C. Chen, K.H. Chen, Nano Lett. 14 (2014) 6097–6103.
[53] M. Tahir, N.S. Amin, Appl. Catal., B 142 (2013) 512–522.
[54] S. Bai, X.J. Wang, C.Y. Hu, M.L. Xie, J. Jiang, Y.J. Xiong, Chem. Commun. 50 (2014) 6094–6097.
[55] Y.Y. Liu, B.B. Huang, Y. Dai, X.Y. Zhang, X.Y. Qin, M.H. Jiang, M.H. Whangbo, Catal. Commun. 11 (2009) 210–213.
[56] Y.A. Wu, I. McNulty, C. Liu, K.C. Lau, Q. Liu, A.P. Paulikas, C.J. Sun, Z.H. Cai, J.R. Guest, Y. Ren, V. Stamenkovic, L.A. Curtiss, Y.Z. Liu, T. Rajh, Nat. Energy 4 (2019) 957–968.
[57] W.G. Tu, Y. Zhou, Q. Liu, S.C. Yan, S.S. Bao, X.Y. Wang, M. Xiao, Z.G. Zou, Adv. Funct. Mater. 23 (2013) 1743–1749.
[58] T.S. Wu, L.Y. Zou, D.X. Han, F.H. Li, Q.X. Zhang, L. Niu, Green Chem. 16 (2014) 2142–2146.
[59] S. Sorcar, J. Thompson, Y. Hwang, Y.H. Park, T. Majima, C.A. Grimes, J.R. Durrant, S.I. In, Energy Environ. Sci. 11 (2018) 3183–3193.
[60] H. Park, H.H. Ou, A.J. Colussi, M.R. Hoffmann, J. Phys. Chem. A 119 (2015) 4658–4666.
[61] J. Mao, T.Y. Peng, X.H. Zhang, K. Li, L.Q. Ye, L. Zan, Catal. Sci. Technol. 3 (2013) 1253–1260.
[62] W. Kim, T. Seok, W. Choi, Energy Environ. Sci. 5 (2012) 6066–6070.
[63] M.S. Hamdy, R. Amrollahi, I. Sinev, B. Mei, G. Mul, J. Am. Chem. Soc. 136 (2014) 594–597.
[64] P. Niu, Y.Q. Yang, J.C. Yu, G. Liu, H.M. Cheng, Chem. Commun. 50 (2014) 10837–10840.
[65] Y. Chen, M.T. Wang, Y.T. Ma, Y.Y. Li, J.Y. Cai, Z.H. Li, Catal. Sci. Technol. 8 (2018) 2218–2223.
[66] N.X. Li, R.M. Jiang, Y. Li, J.C. Zhou, Q.H. Ma, S.H. Shen, M.C. Liu, ACS Sustain. Chem. Eng. 7 (2019) 11455–11463.
[67] Z.W. Chen, H. Zhang, P.J. Guo, J.J. Zhang, G. Tira, Y.J. Kim, Y.M.A. Wu, Y.Z. Liu, J.G. Wen, T. Rajh, J. Niklas, O.G. Poluektov, P.D. Laible, E.A. Rozhkova, J. Am. Chem. Soc. 141 (2019) 11811–11815.
[68] K.K. Sakimoto, A.B. Wong, P.D. Yang, Science 351 (2016) 74–77.
[69] K.K. Sakimoto, S.J. Zhang, P.D. Yang, Nano Lett. 16 (2016) 5883–5887.
[70] H. Zhang, H. Liu, Z. Tian, D. Lu, Y. Yu, S. Cestellos-Blanco, K.K. Sakimoto, P. Yang, Nat. Nanotechnol. 13 (2018) 900.
[71] D. Ren, J.H. Fong, B.S. Yeo, Nat. Commun. 9 (2018) 925.
[72] Y.H. Wang, J.L. Liu, Y.F. Wang, A.M. Al-Enizi, G.F. Zheng, Small 13 (2017) 1701809.
[73] M. Jouny, G.S. Hutchings, F. Jiao, Nat. Catal. 2 (2019) 1062–1070.
[74] A.A. Peterson, F. Abild-Pedersen, F. Studt, J. Rossmeisl, J.K. Norskov, Energy Environ. Sci. 3 (2010) 1311–1315.
[75] T. Cheng, H. Xiao, W.A. Goddard, Proc. Natl. Acad. Sci. U. S. A. 114 (2017) 1795–1800.
[76] A.S. Varela, M. Kroschel, T. Reier, P. Strasser, Catal. Today 260 (2016) 8–13.
[77] Y. Hori, A. Murata, R. Takahashi, J. Chem. Soc., Faraday Trans. 85 (1989) 2309–2326.
[78] K.J.P. Schouten, Z.S. Qin, E.P. Gallent, M.T.M. Koper, J. Am. Chem. Soc. 134 (2012) 9864–9867.
[79] K.J.P. Schouten, E.P. Gallent, M.T.M. Koper, J. Electroanal. Chem. 716 (2014) 53–57.
[80] T.T.H. Hoang, S. Verma, S.C. Ma, T.T. Fister, J. Timoshenko, A.I. Frenkel, P.J.A. Kenis, A.A. Gewirth, J. Am. Chem. Soc. 140 (2018) 5791–5797.
[81] M.G. Kibria, C.T. Dinh, A. Seifitokaldani, P. De Luna, T. Burdyny, R. Quintero-Bermudez, M.B. Ross, O.S. Bushuyev, F.P.G. de Arguer, P.D. Yang, D. Sinton, E.H. Sargen, Adv. Mater. 30 (2018) 1804867.
[82] O.G. Sánchez, Y.Y. Birdja, M. Bulut, J. Vaes, T. Breugelmans, D. Pant, Curr. Opin. Green Sustain. Chem. 16 (2019) 47–56.
[83] Z.Y. Sun, T. Ma, H.C. Tao, Q. Fan, B.X. Han, Chem 3 (2017) 560–587.
[84] Y. Huang, C.W. Ong, B.S. Yeo, ChemSusChem 11 (2018) 3299–3306.
[85] D.F. Gao, I.T. McCrum, S. Deo, Y.W. Choi, F. Scholten, W.M. Wan, J.G.G. Chen, M.J. Janik, B.R. Cuenya, ACS Catal. 8 (2018) 10012–10020.
[86] A. Murata, Y. Hori, Bull. Chem. Soc. Jpn. 64 (1991) 123–127.
[87] J. Resasco, L.D. Chen, E. Clark, C. Tsai, C. Hahn, T.F. Jaramillo, K. Chan, A.T. Bell, J. Am. Chem. Soc. 139 (2017) 11277–11287.
[88] J.H. Montoya, C. Shi, K. Chan, J.K. Nørskov, J. Phys. Chem. Lett. 6 (2015) 2032–2037.
[89] L.D. Chen, M. Urushihara, K. Chan, J.K. Nørskov, ACS Catal. 6 (2016) 7133–7139.
[90] A. Schizodimou, G. Kyriacou, Electrochim. Acta 78 (2012) 171–176.
[91] A.S. Varela, W. Ju, T. Reier, P. Strasser, ACS Catal. 6 (2016) 2136–2144.
[92] Y.G. Kim, J.H. Baricuatro, M.P. Soriaga, Electrocatalysis 9 (2018) 526–530.
[93] Y.G. Kim, J.H. Baricuatro, A. Javier, J.M. Gregoire, M.P. Soriaga, Langmuir 30 (2014) 15053–15056.
[94] D.F. Gao, F. Sohoken, B. Roldan Cuenya, ACS Catal. 7 (2017) 5112–5120.
[95] H. Xiao, W.A. Goddard, T. Cheng, Y.Y. Liu, Proc. Natl. Acad. Sci. U. S. A. 114 (2017) 6685–6688.
[96] D.F. Gao, I. Zegkinoglou, N.J. Divins, F. Scholten, I. Sinev, P. Grosse, B. Roldan Cuenya, ACS Nano 11 (2017) 4825–4831.
[97] S.Y. Lee, H. Jung, N.K. Kim, H.S. Oh, B.K. Min, Y.J. Hwang, J. Am. Chem. Soc. 140 (2018) 8681–8689.
[98] K. Jiang, R.B. Sandberg, A.J. Akey, X.Y. Liu, D.C. Bell, J.K. Norskov, K.R. Chan, H.T. Wang, Nat. Catal. 1 (2018) 111–119.
[99] A. Thevenon, A. Rosas-Hernández, J.C. Peters, T. Agapie, Angew. Chem. Int. Ed. 58 (2019) 16952–16958.
[100] H. Xiao, T. Cheng, W.A. Goddard, J. Am. Chem. Soc. 139 (2017) 130–136.
[101] Y.W. Lum, T. Cheng, W.A. Goddard, J.W. Ager, J. Am. Chem. Soc. 140 (2018) 9337–9340.
[102] E.L. Clark, J. Wong, A.J. Garza, Z. Lin, M. Head-Gordon, A.T. Bell, J. Am. Chem. Soc. 141 (2019) 4191–4193.
[103] Z. Tian, C. Priest, L. Chen, Adv. Theory Simul. 1 (2018) 1800004.
[104] B.A. Rosen, A. Salehi-Khojin, M.R. Thorson, W. Zhu, D.T. Whipple, P.J.A. Kenis, R.I. Masel, Science 334 (2011) 643–644.
[105] X.F. Sun, Q.G. Zhu, X.C. Kang, H.Z. Liu, Q.L. Qian, J. Ma, Z.F. Zhang, G.Y. Yang, B.X. Han, Green Chem. 19 (2017) 2086–2091.
[106] C. Xia, P. Zhu, Q. Jiang, Y. Pan, W. Liang, E. Stavitski, H.N. Alshareef, H. Wang, Nat. Energy 4 (2019) 776–785.
[107] R. Buonsanti, Nat. Energy 4 (2019) 728–729.
[108] C.W. Li, J. Ciston, M.W. Kanan, Nature 508 (2014) 504.
[109] J.E. Pander, D. Ren, Y. Huang, N.W.X. Loo, S.H.L. Hong, B.S. Yeo, ChemElectroChem 5 (2018) 219–237.
[110] H. Mistry, A.S. Varela, C.S. Bonifacio, I. Zegkinoglou, I. Sinev, Y.W. Choi, K. Kisslinger, E.A. Stach, J.C. Yang, P. Strasser, B.R. Cuenya, Nat. Commun. 7 (2016) 12123.
[111] J.Q. Jiao, R. Lin, S.J. Liu, W.C. Cheong, C. Zhang, Z. Chen, Y. Pan, J.G. Tang, K.L. Wu, S.F. Hung, H.M. Chen, L.R. Zheng, Q. Lu, X. Yang, B.J. Xu, H. Xiao, J. Li, D.S. Wang, Q. Peng, C. Chen, Y.D. Li, Nat. Chem. 11 (2019) 222–228.
[112] Y.S. Zhou, F.L. Che, M. Liu, C.Q. Zou, Z.Q. Liang, P. De Luna, H.F. Yuan, J. Li, Z.Q. Wang, H.P. Xie, H.M. Li, P.N. Chen, E. Bladt, R. Quintero-Bermudez, T.K. Sham, S. Bals, J. Hofkens, D. Sinton, G. Chen, E.H. Sargent, Nat. Chem. 10 (2018) 974–980.
[113] Z. Yin, C. Yu, Z. Zhao, X. Guo, M. Shen, N. Li, M. Muzzio, J. Li, H. Liu, H. Lin, J. Yin, G. Lu, D. Su, S. Sun, Nano Lett. 19 (2019) 8658–8663.
[114] L. Mandal, K.R. Yang, M.R. Motapothula, D. Ren, P. Lobaccaro, A. Patra, M. Sherburne, V.S. Batista, B.S. Yeo, J.W. Ager, J. Martin, T. Venkatesan, ACS Appl. Mater. Interfaces 10 (2018) 8574–8584.
[115] D. Ren, Y.L. Deng, A.D. Handoko, C.S. Chen, S. Malkhandi, B.S. Yeo, ACS Catal. 5 (2015) 2814–2821.
[116] A. Eilert, F.S. Roberts, D. Friebel, A. Nilsson, J. Phys. Chem. Lett. 7 (2016) 1466–1470.
[117] M. Favaro, H. Xiao, T. Cheng, W.A. Goddard, J. Yano, E.J. Crumlin, Proc. Natl. Acad. Sci. U. S. A. 114 (2017) 6706–6711.
[118] Y.W. Lum, J.W. Ager, Angew. Chem. Int. Ed. 57 (2018) 551–554.
[119] C.W. Lee, K.D. Yang, D.H. Nam, J.H. Jang, N.H. Cho, S.W. Im, K.T. Nam, Adv. Mater. 30 (2018) 1704717.
[120] J.F. He, N.J.J. Johnson, A.X. Huang, C.P. Berlinguette, ChemSusChem 11 (2018) 48–57.
[121] S. Ma, M. Sadakiyo, M. Heima, R. Luo, R.T. Haasch, J.I. Gold, M. Yamauchi, P.J.A. Kenis, J. Am. Chem. Soc. 139 (2017) 47–50.
[122] D. Ren, B.S.H. Ang, B.S. Yeo, ACS Catal. 6 (2016) 8239–8247.
[123] S. Lee, G. Park, J. Lee, ACS Catal. 7 (2017) 8594–8604.
[124] Y. Lum, J.W. Ager, Energy Environ. Sci. 11 (2018) 2935–2944.
[125] C.G. Morales-Guio, E.R. Cave, S.A. Nitopi, J.T. Feaster, L. Wang, K.P. Kuhl, A. Jackson, N.C. Johnson, D.N. Abram, T. Hatsukade, C. Hahn, T.F. Jaramillo, Nat. Catal. 1 (2018) 764–771.
[126] Y.J. Pang, J. Li, Z.Y. Wang, C.S. Tang, P.L. Hsieh, T.T. Zhuang, Z.Q. Liang, C.Q. Zou, X. Wang, P. De Luna, J.P. Edwards, Y. Xu, F.W. Li, C.T. Dinh, M. Zhong, Y.H. Lou, D. Wu, L.J. Chen, E.H. Sargent, D. Sinton, Nat. Catal. 2 (2019) 251–258.
[127] Y. Hori, I. Takahashi, O. Koga, N. Hoshi, J. Mol. Catal. A Chem. 199 (2003) 39–47.
[128] K.J.P. Schouten, E.P. Gallent, M.T.M. Koper, ACS Catal. 3 (2013) 1292–1295.
[129] Y. Wang, H. Shen, K.J.T. Livi, D. Raciti, H. Zong, J. Gregg, M. Onadeko, Y. Wan, A. Watson, C. Wang, Nano Lett. 19 (2019) 8461–8468.

[130] A. Loiudice, P. Lobaccaro, E.A. Kamali, T. Thao, B.H. Huang, J.W. Ager, R. Buonsanti, Angew. Chem. Int. Ed. 55 (2016) 5789–5792.
[131] P. Grosse, D.F. Gao, F. Scholten, I. Sinev, H. Mistry, B. Roldan Cuenya, Angew. Chem. Int. Ed. 57 (2018) 6192–6197.
[132] Y.X. Duan, F.L. Meng, K.H. Liu, S.S. Yi, S.J. Li, J.M. Yan, Q. Jiang, Adv. Mater. 30 (2018) 1706194.
[133] M. Ma, K. Djanashvili, W.A. Smith, Angew. Chem. Int. Ed. 55 (2016) 6680–6684.
[134] D. Raciti, M. Mao, C. Wang, Nanotechnology 29 (2018), 044001.
[135] D. Raciti, M. Mao, J.H. Park, C. Wang, Catal. Sci. Technol. 8 (2018) 2364–2369.
[136] A. Dutta, M. Rahaman, N.C. Luedi, P. Broekmann, ACS Catal. 6 (2016) 3804–3814.
[137] D. Raciti, C. Wang, ACS Cent. Sci. 3 (2018) 1545–1556.
[138] A. Verdaguer-Casadevall, C.W. Li, T.P. Johansson, S.B. Scott, J.T. McKeown, M. Kumar, I.E.L. Stephens, M.W. Kanan, I. Chorkendorff, J. Am. Chem. Soc. 137 (2015) 9808–9811.
[139] X.F. Feng, K.L. Jiang, S.S. Fan, M.W. Kanan, ACS Cent. Sci. 2 (2016) 169–174.
[140] T. Cheng, H. Xiao, W.A. Goddard, J. Am. Chem. Soc. 139 (2017) 11642–11645.
[141] S. Ahn, K. Klyukin, R.J. Wakeham, J.A. Rudd, A.R. Lewis, S. Alexander, F. Carla, V. Alexandrov, E. Andreoli, ACS Catal. 8 (2018) 4132–4142.
[142] Z.J. Han, R. Kortlever, H.Y. Chen, J.C. Peters, T. Agapie, ACS Cent. Sci. 3 (2017) 853–859.
[143] F. Li, A. Thevenon, A. Rosas-Hernández, Z. Wang, Y. Li, C.M. Gabardo, A. Ozden, C.T. Dinh, J. Li, Y. Wang, J.P. Edwards, Y. Xu, C. McCallum, L. Tao, Z.-Q. Liang, M. Luo, X. Wang, H. Li, C.P. O'Brien, C.-S. Tan, D.-H. Nam, R. Quintero-Bermudez, T.-T. Zhuang, Y.C. Li, Z. Han, R.D. Britt, D. Sinton, T. Agapie, J.C. Peters, E.H. Sargent, Nature 577 (2019) 509–513.
[144] S.A. Francis, J.M. Velazquez, I.M. Ferrer, D.A. Torelli, D. Guevarra, M.T. McDowell, K. Sun, X.H. Zhou, F.H. Saadi, J. John, M.H. Richter, F.P. Hyler, K.M. Papadantonakis, B.S. Brunschwig, N.S. Lewis, Chem. Mater. 30 (2018) 4902–4908.
[145] J.J. Wu, S.C. Ma, J. Sun, J.I. Gold, C. Tiwary, B. Kim, L.Y. Zhu, N. Chopra, I.N. Odeh, R. Vajtai, A.Z. Yu, R. Luo, J. Lou, G.Q. Ding, P.J.A. Kenis, P.M. Ajayan, Nat. Commun. 7 (2016) 13869.
[146] Y.M. Liu, S. Chen, X. Quan, H.T. Yu, J. Am. Chem. Soc. 137 (2015) 11631–11636.
[147] C. Genovese, M.E. Schuster, E.K. Gibson, D. Gianolio, V. Posligua, R. Grau-Crespo, G. Cibin, P.P. Wells, D. Garai, V. Solokha, S.K. Calderon, J.J. Velasco-Velez, C. Ampelli, S. Perathoner, G. Held, G. Centi, R. Arrigo, Nat. Commun. 9 (2018) 935.
[148] T.T. Zhuang, D.H. Nam, Z.Y. Wang, H.H. Li, C.M. Gabardo, Y. Li, Z.Q. Liang, J. Li, X.J. Liu, B. Chen, W.R. Leow, R. Wu, X. Wang, F.W. Li, Y. Lum, J. Wicks, C.P. O'Brien, T. Peng, A.H. Ip, T.K. Sham, S.H. Yu, D. Sinton, E.H. Sargent, Nat. Commun. 10 (2019) 1807.
[149] Y. Liu, Y. Zhang, K. Cheng, X. Quan, X. Fan, Y. Su, S. Chen, H. Zhao, Y. Zhang, H. Yu, M.R. Hoffmann, Angew. Chem. Int. Ed. 56 (2017) 15607–15611.
[150] D. Sun, X. Xu, Y. Qin, S.P. Jiang, Z. Shao, ChemSusChem 13 (2019) 39–58.
[151] Y. Song, S. Wang, W. Chen, S. Li, G. Feng, W. Wei, Y. Sun, ChemSusChem 13 (2019) 293–297.
[152] H. Yamashita, K. Ikeue, T. Takewaki, M. Anpo, Top. Catal. 18 (2002) 95–100.
[153] K. Manthiram, B.J. Beberwyck, A.P. Aivisatos, J. Am. Chem. Soc. 136 (2014) 13319–13325.
[154] K.P. Kuhl, E.R. Cave, D.N. Abram, T.F. Jaramillo, Energy Environ. Sci. 5 (2012) 7050–7059.
[155] R. Kas, R. Kortlever, A. Milbrat, M.T.M. Koper, G. Mul, J. Baltrusaitis, Phys. Chem. Chem. Phys. 16 (2014) 12194–12201.
[156] D. Ren, N.T. Wong, A.D. Handoko, Y. Huang, B.S. Yeo, J. Phys. Chem. Lett. 7 (2016) 20–24.
[157] Y. Kwon, Y.W. Lum, E.L. Clark, J.W. Ager, A.T. Bell, ChemElectroChem 3 (2016) 1012–1019.
[158] Y.W. Lum, B.B. Yue, P. Lobaccaro, A.T. Bell, J.W. Ager, J. Phys. Chem. C 121 (2017) 14191–14203.
[159] C.S. Chen, A.D. Handoko, J.H. Wan, L. Ma, D. Ren, B.S. Yeo, Catal. Sci. Technol. 5 (2015) 161–168.
[160] M. Ma, K. Djanashvili, W.A. Smith, Phys. Chem. Chem. Phys. 17 (2015) 20861–20867.
[161] C.W. Li, M.W. Kanan, J. Am. Chem. Soc. 134 (2012) 7231–7234.
[162] K. Gupta, M. Bersani, J.A. Darr, J. Mater. Chem. A 4 (2016) 13786–13794.